



HAL
open science

Falling liquid films in narrow tubes: occlusion scenarios

Georg Dietze, G. Lavalley, C. Ruyey-Quil

► **To cite this version:**

Georg Dietze, G. Lavalley, C. Ruyey-Quil. Falling liquid films in narrow tubes: occlusion scenarios. Journal of Fluid Mechanics, 2020, 894, 10.1017/jfm.2020.267 . hal-03044949

HAL Id: hal-03044949

<https://hal.science/hal-03044949>

Submitted on 7 Dec 2020

HAL is a multi-disciplinary open access archive for the deposit and dissemination of scientific research documents, whether they are published or not. The documents may come from teaching and research institutions in France or abroad, or from public or private research centers.

L'archive ouverte pluridisciplinaire **HAL**, est destinée au dépôt et à la diffusion de documents scientifiques de niveau recherche, publiés ou non, émanant des établissements d'enseignement et de recherche français ou étrangers, des laboratoires publics ou privés.

Falling liquid films in narrow tubes: occlusion scenarios

Georg F. Dietze^{1†}, G. Lavallo² and C. Ruyer-Quil³

¹Université Paris-Saclay, CNRS, FAST, 91405, Orsay, France.

²Université Paris-Saclay, CNRS, LIMSI, 91405, Orsay, France.

³Université Savoie Mont Blanc

(Received 26 February 2020; revised xx; accepted xx)

We study a gravity-driven wavy liquid film falling down the inner surface of a narrow cylindrical tube in the presence of an active core gas flow. We employ the model of Dietze and Ruyer-Quil (*J. Fluid Mech.*, vol. 762, 2015, pp. 68-109) to investigate the role of surface waves in the occlusion of the tube. We consider four real working liquids and reproduce several experiments from the literature, focusing on conditions where the Bond number is greater or equal to unity. We prove that occlusion is triggered by spatially growing surface waves beyond the limit of saturated travelling-wave solutions, and **delimit** three possible regimes for a naturally evolving wavy film: (i) certain occlusion, when the liquid Reynolds number is greater than the limit of the spatially most-amplified travelling waves. Occlusion is caused by surface waves emerging from linear wave selection (scenario I); (ii) conditional occlusion, when the most-amplified waves possess travelling states but longer waves don't. Occlusion is triggered by secondary instability, generating long waves through nonlinear coarsening dynamics (scenario II); and (iii) impossible occlusion, when travelling waves always exist, no matter how great their wavelength. We show that certain occlusion is delayed by gravity and precipitated by a counter-current gas flow, axial viscous diffusion (high-viscosity liquids), and inertia (low-viscosity liquids). The latter two effects are also found to determine whether the occlusion mechanism is dictated by loss of travelling-wave solutions or absolute instability. Finally, we show that occlusion can be prevented through coherent inlet forcing. As a side benefit, we introduce an augmented version of our model based on a localized additional force term that allows representing stable travelling liquid pseudo-plugs.

Key words: Thin films

1. Introduction

We consider the configuration in figure 1, a thin liquid film falling down the inner surface of a vertical cylindrical tube of radius R^* under the action of the gravitational acceleration g . The film of liquid (denoted with the subscript l) is in contact with a laminar flow of gas in the core (subscript g). Both fluids are assumed to be Newtonian with constant densities ρ_l and ρ_g , dynamic viscosities μ_l and μ_g , and surface tension σ . Also, we assume the arrangement to be axisymmetric. We denote the film thickness h , the core radius d , its spatial average \bar{d} , and the flow rates q_l and q_g . Their dimensional

† Email address for correspondence: dietze@fast.u-psud.fr

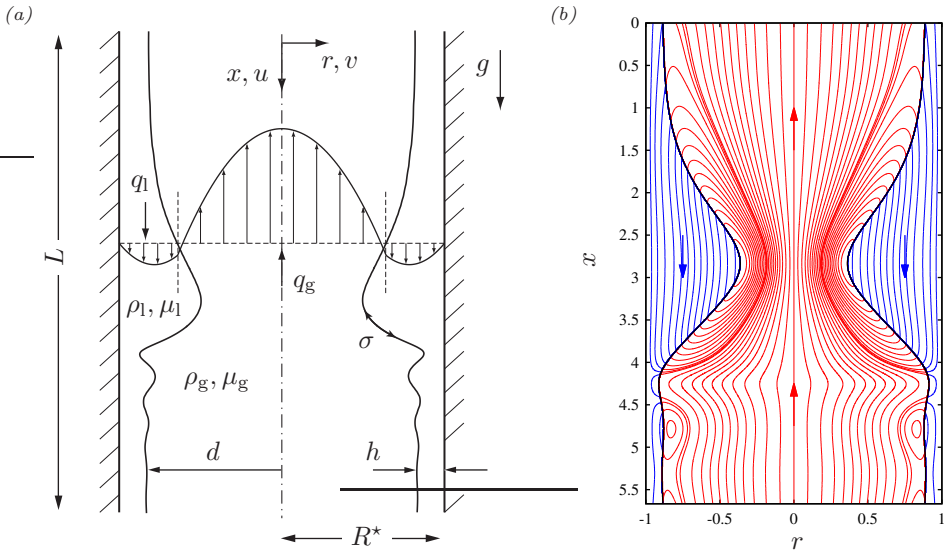


FIGURE 1. Falling liquid film (subscript l) lining the inner surface of a narrow cylindrical tube in contact with a laminar gas flow in the core (subscript g). (a) Problem configuration and notations. The tube radius R^* is the length scale, the star superscript designating dimensional quantities; (b) example of a travelling-wave computation with our model (2.5): case 4 in table 1 (low-viscosity silicone oil), $Re=14.6$, $Re_g=-17.27$ (limit point marked by asterisk in panel 13a). Streamlines in the wall-fixed reference frame within the liquid (blue lines) and gas (red lines).

38 counterparts will be distinguished by a star, e.g. d^* , and their counterparts in the
 39 corresponding flat-film primary flow will be denoted with a subscript zero, e.g. d_0 .

40 We focus on conditions, where: (i) the effect of gravity, quantified through the **Bond**
 41 **number** $Bo=\rho_l g R^{*2}/\sigma$, is at least comparable to that of capillarity ($Bo \geq 1$); (ii) the
 42 liquid film's inertia, quantified through the **Reynolds number** $Re=q_{l0}^* \rho_l / (\pi R^* \mu_l)$, is not
 43 necessarily negligible ($Re \leq 20$); and (iii) the effect of the gas flow can be relevant, but
 44 its Reynolds number $Re_g=q_{g0}^* \rho_g / (\pi R^* \mu_g)$ remains moderate ($|Re_g| < 20$).

45 We investigate this flow with the weighted residual integral boundary layer (WRIBL)
 46 model of Dietze & Ruyer-Quil (2015), which was previously applied only to gravity-free
 47 films. The model accounts for gravity, inertia, full interfacial curvature, axial viscous
 48 diffusion, and full inter-phase coupling. Our model computations are confronted with
 49 our own direct numerical simulations (DNS) in appendix A and panel 5d.

50 We focus on the occlusion of the narrow tube due to the interfacial instability of the
 51 falling liquid film, as observed experimentally by Dao & Balakotaiah (2000) and Camassa
 52 *et al.* (2014). Occlusion is relevant for chemical engineering applications such as tubular
 53 falling film micro-reactors (Seebauer *et al.* 2012). It also occurs in the human pulmonary
 54 airways due to the collapse of the mucus-serous film lining their inner surface (Grotberg
 55 2011). In the lower generations of bronchioles, the effect of gravity and possibly inertia
 56 is not necessarily negligible (Kamm & Schroter 1989).

57 The falling liquid film is subject to two instability mechanisms causing interfacial
 58 deformations: the Plateau-Rayleigh mechanism (Plateau 1849; Rayleigh 1892; Goren
 59 1962), due to the azimuthal curvature of the film surface; and the Kapitza mechanism
 60 (Kapitza 1948), due to inertia, which sets in as a result of the gravity-driven mean flow
 61 (Brooke Benjamin 1957; Yih 1963). The strength of this mean flow determines whether

the absolute nature of the Plateau-Rayleigh instability or the convective nature of the Kapitza instability dominates (Duprat *et al.* 2007). For the liquids studied here, we find that occlusion is dictated by absolute instability when $Bo \ll 1$, whereas convective instability is responsible for occlusion when $Bo \geq 1$.

In the case of convective instability, the liquid film can produce travelling surface waves, which remain stationary in their reference frame. Gravity plays an important role in shaping these waves, compressing the leading and elongating the trailing wave front, which results in asymmetric tear-shaped wave humps (Dietze 2016). The resulting distortion of the film surface favours variations in axial (stabilizing) over azimuthal (destabilizing) surface curvature. In related systems, this mechanism has been found to saturate the Plateau-Rayleigh instability in the weakly-nonlinear regime (Frenkel *et al.* 1987), to the extent that the film looks stable to the naked eye (Quéré 1990). In our current problem, we find that it greatly extends the region of existence of strongly-nonlinear travelling waves and considerably delays occlusion.

Trifonov (1992) applied the integral boundary layer approach of Shkadov (1967) to model an annular liquid film falling in a vertical cylindrical tube. The author found that the Plateau-Rayleigh mechanism systematically increases the amplitude of travelling waves versus a planar falling liquid film, where only the Kapitza mechanism is active. He also observed *catastrophic growth*, when the amplitude of travelling-wave solutions diverged as a function of $1/R$. In those instances, the effect of gravity was negligible, i.e. $Bo \ll 1$. By contrast, we focus on occlusion in the limit $Bo \geq 1$. Moreover, the model of Trifonov (1992) did not account for axial viscous diffusion, which we find to greatly precipitate occlusion in high-viscosity films.

Dao & Balakotaiah (2000) performed falling-film experiments in long narrow tubes and determined the occlusion onset in terms of Re for a wide range of liquids. However, no information was available on the wave dynamics responsible for occlusion. By reproducing two of these experiments (runs 13 and 20 there) with our own spatio-temporal computations, we provide this missing information, leading us to distinguish two wave-induced occlusion scenarios. In scenario I, waves causing occlusion emerge directly from linear wave selection. In scenario II, they result from the secondary instability of a regular train of travelling waves, triggering a cascade of coalescence/absorption events that produce increasingly long, more dangerous, waves. The secondary instability (Liu & Gollub 1993) and the ensuing cascaded coarsening dynamics (Chang *et al.* 1996*b*) are well known phenomena in planar falling liquid films.

Jensen (2000) investigated annular collars travelling on a gravity-driven liquid film lining the inner surface of a cylindrical tube. The collars were constructed from unduloids, i.e. symmetric constant-curvature equilibrium shapes (Delaunay 1841). The author studied under what conditions collars may grow to occlude the tube. Our study extends this work in that the collar shape is not forced to be symmetric, but follows implicitly from the evolution equations. This allows for the gravity-induced distortion of collars, which we find can greatly delay occlusion.

Camassa *et al.* (2014) performed falling-film occlusion experiments in a transparent tube, using a [high-viscosity silicone oil](#). By confronting these with linear stability calculations, the authors concluded that occlusion is caused by spatially growing nonlinear waves and not by absolute linear instability ($Bo=11.06$ in their experiments). Further, with the help of a first-order long-wave model obtained from asymptotic expansion (Benney 1966), the authors constructed travelling-wave solutions. By continuing these at fixed wave length in terms of Re , they identified a limit point (LP), and conjectured that this may signal the occlusion onset in a real system. **However, the authors cautioned that further work was needed to verify this w.r.t. their experiments. This work was initiated**

112 by Camassa *et al.* (2016), but their model did not account for axial viscous diffusion,
 113 which we show to strongly affect travelling wave solutions, and the wavelength assumed
 114 in their continuation was too long compared to the experiment.

115 In our current study, we have checked the conjecture of Camassa *et al.* (2014) based on
 116 travelling-wave and spatio-temporal computations with our model. We have successfully
 117 confronted these computations with the experiments of Camassa *et al.* (2014) and find
 118 that accounting for axial viscous diffusion greatly improves agreement. Based on our
 119 computations, we find that the surface waves causing occlusion indeed systematically
 120 lie beyond the limit of travelling-wave solutions (figure 4), confirming the conjecture of
 121 Camassa *et al.* (2014). This limit is highly sensitive to the considered wavelength, long
 122 waves being more dangerous than short ones, as shown by Camassa *et al.* (2016) and
 123 Ding *et al.* (2019). Thus, any predictive criterion for occlusion based on travelling-wave
 124 solutions must account for the type of waves that actually occur in a real system.

125 For this, we introduce the upper conservative occlusion bound Re_{\max} , which corre-
 126 sponds to the limit point of travelling-wave solutions at the spatially most amplified
 127 frequency of linear waves f_{\max} . For $Re > Re_{\max}$, the most amplified surface waves, which
 128 typically emerge in an experiment, do not possess travelling states and occlusion is certain
 129 to occur in a naturally evolving film. We find that the occlusion experiments of Camassa
 130 *et al.* (2014) and experimental run 20 in Dao & Balakotaiah (2000) correspond to this
 131 regime. Occlusion in this case occurs through scenario I. To determine Re_{\max} , we have
 132 computed the most amplified wave frequency f_{\max} in our numerical continuations by
 133 solving the linear spatial stability problem along with our nonlinear model equations.
 134 This had not been attempted by Camassa *et al.* (2014) and Ding *et al.* (2019).

135 At the other end, occlusion is delimited by a lower conservative bound $Re = Re_0$, below
 136 which travelling wave solutions always exist, no matter how great the wavelength, and
 137 occlusion is impossible. The existence of such a limit was discovered by Ding *et al.* (2019).

138 We find that the conservative occlusion bounds Re_0 and Re_{\max} delimit a region of
 139 conditional occlusion, $Re_0 < Re < Re_{\max}$, where occlusion is theoretically possible (for long
 140 enough waves) but does not necessarily occur in a real system. Whether it does, depends
 141 on the specific wave dynamics that unfolds over the spatio-temporal evolution of the
 142 film, and whether the tube is long enough to accommodate this. In this regime, we find
 143 that occlusion is caused by scenario II and that it applies to experimental run 13 in
 144 Dao & Balakotaiah (2000). It also opens the possibility of preventing occlusion through
 145 coherent inlet forcing, i.e. by forcing waves of sufficiently high frequency. We validate this
 146 idea based on spatio-temporal computations.

147 Unless Bo is very large, we find that the height of travelling waves at the limit point
 148 $Re = Re_{\max}$ is far from reaching the tube radius. In contrast to what Dao & Balakotaiah
 149 (2000) conjectured, travelling-wave solutions are thus lost abruptly and not due to the
 150 wave height reaching the tube radius continuously.

151 Zhou *et al.* (2016) investigated viscoelastic liquid films falling in a deformable narrow
 152 tube. The authors performed calculations with a model based on the same approach
 153 as Trifonov (1992), which does not account for axial viscous diffusion. Interestingly,
 154 it was shown that occlusion can cause a contraction of the flexible tube. Such events
 155 are known to occur in the pulmonary airways (Grotberg 2011) and can damage cells
 156 within the capillaries (Bian *et al.* 2010). The authors went on to determine the occlusion
 157 onset by varying the liquid flow rate in spatio-temporal computations. This onset was
 158 defined as the point at which the computation breaks down due to an occlusion event.
 159 However, such computations cannot attain a representative developed state. For example,
 160 when starting from a flat-film initial condition, a single unrealistically large tsunami-like
 161 wave usually develops in the early stages. This wave is bound to cause occlusion, but

162 it is not representative of a real system. By contrast, we characterize occlusion based
 163 on the bounds Re_0 and Re_{\max} of travelling-wave solutions, and our spatio-temporal
 164 computations have all been continued until reaching a statistically-developed state. To
 165 achieve this, we have allowed our computations to continue past occlusion events by
 166 numerically limiting the core radius of an occluded region to a small but finite value.

167 Liu & Ding (2017) studied a vertically falling glycerol film flowing down a porous
 168 cylindrical surface using a lubrication equation. The authors found that porosity pre-
 169 cipitates both the absolute instability threshold and the occlusion limit. Using the same
 170 approach, Ding *et al.* (2019) studied the effect of the Marangoni instability on a radially-
 171 heated liquid film falling in a vertical cylindrical tube. The authors found that Marangoni
 172 stresses promote/delay occlusion when the film is heated/cooled from the wall. However,
 173 their modelling approach does not account for inertia nor axial viscous diffusion. We find
 174 that this does not allow to accurately predict occlusion in high-viscosity (because of axial
 175 viscous diffusion) or low-viscosity (because of inertia) liquids.

176 The model employed in our current study extends upon the earlier works of Trifonov
 177 (1992), Camassa *et al.* (2014, 2017), Zhou *et al.* (2016), Liu & Ding (2017), and Ding
 178 *et al.* (2019) by accounting for axial viscous diffusion and inertia. This has allowed us to
 179 investigate four real liquids, for which we determine the lower and upper occlusion bounds
 180 Re_0 and Re_{\max} and characterize the possible occlusion scenarios. When the viscosity is
 181 high, we find that axial viscous diffusion greatly precipitates the upper occlusion bound
 182 Re_{\max} (by 74% for the high-viscosity silicone oil). When the viscosity is low (low-viscosity
 183 silicone oil), inertia cannot be neglected and is found to precipitate Re_{\max} by 20%. We
 184 also find that these two effects determine whether the occlusion mechanism is dictated
 185 by absolute linear instability or the loss of travelling-wave solutions.

186 Our model also accounts for full inter-phase coupling between the liquid and gas,
 187 and this has allowed us to study the effect of a laminar counter-current gas flow on
 188 the occlusion bound Re_{\max} . For low-viscosity liquids, where the wave-induced pressure
 189 variation in the gas becomes relevant in the liquid force balance, we find that Re_{\max} is
 190 significantly reduced with increasing $|Re_g|$ (by up to 25% in our computations). Thereby,
 191 the conditions we have studied differ from previous works. Alekseenko *et al.* (2009)
 192 experimentally studied the linear stability of a falling liquid film subject to a co-current
 193 turbulent gas flow. Their tube radius was large and thus occlusion could not occur.
 194 Camassa *et al.* (2012, 2017) studied co-current upward liquid/gas flows based on a long-
 195 wave model, where the effect of the (turbulent) gas flow was accounted for by relaxing the
 196 inter-phase coupling conditions in the limit of high gas velocities. By contrast, we focus
 197 on laminar (counter-current) gas flows, where our model, which relies on the unrelaxed
 198 coupling conditions, behaves well.

199 For the case of a planar falling liquid film sheared by a confined gas flow, many works
 200 have investigated the flooding phenomenon, where the liquid film either occludes the
 201 channel (Vlachos *et al.* 2001), surface waves (Tseluiko & Kalliadasis 2011) or the liquid
 202 flow (Trifonov 2010) reverse direction, or the liquid film disintegrates into drops (Zapke
 203 & Kröger 2000).

204 Finally, several works are related less directly to the studied problem. Kouris &
 205 Tsamopoulos (2001) studied liquid/liquid gravity-driven flows through a vertical pipe.
 206 Beltrame (2018) studied the transition between partial and complete wetting in a micro-
 207 tube. Xu & Jensen (2017) studied migration of liquid films in tubes with rough walls.
 208 Moreover, many works have dealt with pressure-driven core-annular flows (Aul & Olbricht
 209 1990; Joseph *et al.* 1997) or liquid films falling down fibres (Kalliadasis & Chang 1994;
 210 Quéré 1999). In the latter case, occlusion cannot occur, unless the gas phase is confined
 211 by an additional concentric hollow cylinder (Wray 2013).

Our manuscript is structured as follows. Section 2 introduces the governing equations, and details of our model (§2.1), direct numerical simulations (§2.2), and linear stability calculations (§2.3). Results are presented in §3, where we start by proving that occlusion in real systems results from surface waves that lie beyond the limit of travelling-wave solutions (§3.1). In §3.2, we compute the upper and lower occlusion bounds Re_{max} and Re_0 , delimiting the regimes of certain, conditional, and impossible occlusion. **For one of the studied cases, we validate these results based on our own DNS of travelling-wave solutions.** In sections 3.3 to 3.6, we show how Re_{max} is affected by gravity, axial viscous diffusion, inertia, and the core gas flow. In §3.7, we demonstrate occlusion scenarios I (certain occlusion regime) and II (conditional occlusion regime) by reproducing two of the experimental runs from Dao & Balakotaiah (2000) with spatio-temporal computations. In §3.8, we show that occlusion in the conditional regime can be prevented through coherent inlet forcing. Conclusions are drawn in §4. **The appendix reports comparisons with transient DNS (appendix A), numerical details regarding our travelling-wave DNS (appendix B), as well as additional discussions of panels 13a (appendix C) and 4a (appendix D). Finally, appendix E introduces an augmented version of our WRIBL model that allows a better representation of liquid plugs, based on a localized force term.**

2. Mathematical description

We consider the flow in panel 1a, which is rotationally symmetric w.r.t. the tube axis, and is governed by the Navier-Stokes and continuity equations for the liquid (subscript $k=l$, $\chi_l=1$) and gas (subscript $k=g$, $\chi_g=\Pi_\mu/\Pi_\rho$):

$$d_t u_k = -\partial_x p_k + \text{Fr}^{-2} + \chi_k \text{Re}^{-1} \{ r^{-1} \partial_r (r \partial_r u) + \partial_{xx} u \}, \quad (2.1a)$$

$$d_t v_k = -\partial_r p_k + \chi_k \text{Re}^{-1} \{ \partial_r [r^{-1} \partial_r (r v)] + \partial_{xx} v \},$$

$$\partial_x u_k + r^{-1} \partial_r (v_k r) = 0, \quad (2.1b)$$

where $\text{Re}=\rho_l \mathcal{U} \mathcal{L} / \mu_l = q_{l0}^* / (\pi R^*) / (\mu_l / \rho_l)$ is the Reynolds number and $\text{Fr}=\mathcal{U} / \sqrt{g \mathcal{L}}$ is the Froude number, all variables having been rendered dimensionless with the following reference scales: the length scale $\mathcal{L}=R^*$, which corresponds to the tube radius, the velocity scale $\mathcal{U}=q_{l0}^* / \pi / R^{*2}$, which corresponds to the surface velocity of the liquid, the time scale $\mathcal{T}=\mathcal{L} / \mathcal{U}$, and the pressure scale $\mathcal{P}_k=\rho_k \mathcal{U}^2$, which corresponds to the phase-specific dynamical pressure. The star symbol denotes dimensional quantities, and the subscript zero the flat-film primary flow. Thus, q_{l0} designates the nominal liquid flow rate.

The set of governing equations is completed by the boundary conditions:

$$u_l|_{r=R} = v_l|_{r=R} = 0, \quad \partial_r u_g|_{r=0} = v_g|_{r=0} = 0, \quad (2.2)$$

and the kinematic/dynamic inter-phase coupling conditions at the film surface $r=d$:

$$u_l = u_g, \quad v_l = v_g = \partial_t d + u_k \partial_x d, \quad (2.3a)$$

$$\tau_1^t = \Pi_\mu \tau_g^t, \quad (2.3b)$$

$$\tau_k^t = \partial_r u_k + \partial_x v_k - 2 \partial_x d (1 + \partial_x d^2)^{-1} [\partial_x u_k - \partial_r v_k],$$

$$\tau_1^n + \text{Re} p_l = \Pi_\mu \tau_g^n + \Pi_\rho \text{Re} p_g + \text{Re} \text{We}^{-1} \kappa, \quad (2.3c)$$

$$\tau_k^n = 2 (1 + \partial_x d^2)^{-1} [\partial_x d \partial_r u_k - \partial_r v_k - \partial_x d^2 \partial_x u_k + \partial_x d \partial_x v_k],$$

where τ^t and τ^n designate the tangential and normal interfacial viscous stresses, $\Pi_\rho=\rho_g/\rho_l$ and $\Pi_\mu=\mu_g/\mu_l$ are the density and dynamic viscosity ratios, $\text{We}=\rho_l \mathcal{U}^2 \mathcal{L} / \sigma$ is

247 the Weber number, and κ denotes the total curvature of the film surface:

$$\kappa = \partial_{xx}d - \frac{1}{d} \left[1 - \frac{1}{2} (\partial_x d)^2 \right]. \quad (2.4)$$

248 We will refer to computations based on the full equations (2.1) to (2.3) as direct
 249 numerical simulations (DNS). These have been performed for validation purposes and
 250 results are reported in appendix A and panel 5d. However, most of our computations
 251 were carried out with the weighted residual integral boundary layer (WRIBL) model of
 252 Dietze & Ruyer-Quil (2015), which we introduce next.

253 2.1. Weighted residual integral boundary layer (WRIBL) model

254 The WRIBL model consists of three coupled partial differential equations for the core
 255 radius d , and the flow rates q_l and q_g (Dietze & Ruyer-Quil 2015):

$$\partial_x q_j - \varepsilon_j 2\pi d \partial_t d = 0, \quad (2.5a)$$

$$\begin{aligned} \{S_i \partial_t q_i + F_{ij} q_i \partial_x q_j + G_{ij} q_i q_j \partial_x d\} = \text{Fr}^{-2} (1 - \Pi_\rho) \\ - \text{We}^{-1} \partial_x [\kappa] + \text{Re}^{-1} (C_{jl} - \Pi_\mu C_{jg}) q_j \\ + \text{Re}^{-1} \left\{ J_j q_j (\partial_x d)^2 + K_j \partial_x q_j \partial_x d + L_j q_j \partial_{xx} d + M_j \partial_{xx} q_j \right\}, \end{aligned} \quad (2.5b)$$

257 where the subscripts i and j are to be permuted over the phase indicators for the liquid
 258 ($i, j=1$) and gas ($i, j=g$). This yields two equations from (2.5a), ensuring integral mass
 259 conservation, and one equation from (2.5b), which ensures conservation of momentum.
 260 The RHS terms in (2.5b) account for different driving forces, i.e. gravity, capillarity, and
 261 viscous drag. Relating these terms directly to one another yields two alternative dimensionless
 262 groups that are also useful for characterizing the studied flow regimes: the Bond
 263 number $\text{Bo} = \text{We} \text{Fr}^{-2} = \rho_l g R^{*2} / \sigma$, which relates gravity to capillarity, and the capillary
 264 number $\text{Ca} = \text{We} / \text{Re} = \mu_l \mathcal{U} / \sigma$, which relates viscous drag to capillarity. Following Dao &
 265 Balakotaiah (2000), we will also make use of the Kapitza number $\text{Ka} = \sigma \rho_l^{-1} g^{-1/3} \mu_l^{-4/3}$,
 266 and the Laplace number $\text{La} = \sigma \rho_l R^* / \mu_l^2$. We point out however that the list Re , Fr , We ,
 267 Bo , Ca , Ka , and La , contains only three independent dimensionless groups, e.g. Re , Ka ,
 268 and Bo , which (along with Π_μ and Π_ρ) suffice to fully describe the flow. All other groups
 269 can be expressed in terms of these three, e.g. $\text{Ca} = \text{Re}(\text{BoKa}^3)^{-1/2}$.

270 The model is completed by an equation for the gas pressure gradient $\partial_x p_g|_{r=d}$:

$$\begin{aligned} 2 \Pi_\rho \text{Re} \partial_x p_g|_{r=d} = -\text{Re} \{ \underline{S}_i \partial_t q_i + \underline{F}_{ij} q_i \partial_x q_j + \underline{G}_{ij} q_i q_j \partial_x d \} \\ + \text{Re} \text{Fr}^{-2} (1 + \Pi_\rho) - \text{We}^{-1} \text{Re} \partial_x [\kappa] + (C_{jl} + \Pi_\mu C_{jg}) q_j \\ + \underline{J}_j q_j (\partial_x d)^2 + \underline{K}_j \partial_x q_j \partial_x d + \underline{L}_j q_j \partial_{xx} d + \underline{M}_j \partial_{xx} q_j, \end{aligned} \quad (2.5c)$$

271 which is used either to evaluate the pressure distribution a posteriori or to impose a gas
 272 pressure drop through an integral condition. The coefficients F_{ij} , G_{ij} , C_{ij} , S_j , J_j , K_j ,
 273 and M_j in (2.5b) and their counterparts marked by an underscore in (2.5c) are known
 274 functions of d . They can be found in appendix A of Dietze & Ruyer-Quil (2015).

275 We solve the equation system (2.5) numerically using three approaches: (i) transient
 276 periodic computations, where the domain length L corresponds to the wavelength Λ and
 277 where $\partial_x^i q_k|_{x=0} = \partial_x^i q_k|_{x=\Lambda}$ and $\partial_x^i d|_{x=0} = \partial_x^i d|_{x=\Lambda}$ for $i=0,1,2,3$. The code employed for
 278 this is based on a Crank-Nicolson time discretization and first-order central differences for
 279 spatial discretization (Dietze & Ruyer-Quil 2015); (ii) continuation of periodic travelling
 280 wave solutions that are stationary in the wave-fixed coordinate $\xi = x - ct$ moving with
 281 the wave celerity c . These computations were performed with the continuation software
 282 AUTO07P (Doedel 2008); (iii) transient open-domain computations with inlet and outlet

283 conditions. At the liquid inlet, $x=0$, we fix the core radius $d=d_0$ of the flat-film primary
 284 flow. For the liquid flow rate q_l , we superimpose a zero-mean temporal perturbation on
 285 the nominal value q_{l0} :

$$q_l(x=0, t) = q_{l0} [1 + F(t)], \quad (2.6a)$$

286 where the function $F(t)$ defines the type of inlet perturbation:

$$F(t) = \epsilon_1 \sin(2\pi f t) + \epsilon_2 \sum_{k=1}^N \sin(2\pi k \Delta f t + \varphi_{\text{rand}}), \quad \Delta f = 2 f_c/N. \quad (2.6b)$$

287 The first term in (2.6b) constitutes a harmonic perturbation of frequency f and the second
 288 one mimics white noise through a series of $N=1000$ Fourier modes that are shifted by
 289 a random phase shift $\varphi_{\text{rand}}=\varphi_{\text{rand}}(k) \in [0, 2\pi]$ and that span a frequency range of twice
 290 the linear cut-off frequency f_c (Chang *et al.* 1996a). All our computations were run
 291 with the same $\varphi_{\text{rand}}(k)$ number series, which was generated once and for all with the
 292 pseudo random number generator *RandomReal* in *Mathematica* (2014). The strength of
 293 the two terms in (2.6b) is determined through their amplitudes ϵ_1 and ϵ_2 . When $\epsilon_1=0$, the
 294 inlet perturbation consists only of white noise. This setting will be used to simulate the
 295 natural, noise-driven, evolution of a wavy film as it would occur in an experiment (sections
 296 3.1 and 3.7). In §3.8, we will use coherent inlet forcing to prevent occlusion. In those
 297 computations, we will set $\epsilon_1>0$, thus adding a monochromatic harmonic perturbation to
 298 the inlet noise.

299 At the outlet, $x=L$, we have implemented the boundary conditions of Richard *et al.*
 300 (2016), which ensure that liquid is always sufficiently drained from the domain. We set
 301 $d|_{N+2}=d|_{N+1}=d|_N$, and $q_l|_{N+1}=q_{l0}(R-d|_N)^{3/2}/(R-d_0)^{3/2}$, where N corresponds to the
 302 last grid point within the domain and $N+1$, $N+2$ to the two downstream ghost points.
 303 Computations were started from the initial condition $d(x, t=0)=d_0$, $q_l(x, t=0)=q_{l0}$.

304 In our codes, the gas flow rate q_g is expressed in terms of the total flow rate q_{tot} :

$$q_{\text{tot}}(t) = q_l(x, t) + q_g(x, t), \quad (2.7)$$

305 which is spatially invariant. In our computations, we either fix q_{tot} explicitly, which fixes
 306 the nominal gas flow rate q_{g0} , given a nominal liquid flow rate q_{l0} . Or, q_{tot} is dynamically
 307 adjusted to produce a fixed gas pressure drop Δp_g , imposed through an integral condition
 308 on (2.5c). We quantify this pressure drop through the normalized pressure gradient:

$$\Psi = \Delta p_g / L \text{Fr}^2, \quad (2.8)$$

309 where L is the domain length. When $\Psi=1$, the pressure drop exactly balances the weight
 310 of the gas column, and we refer to this as the aerostatic situation. This is most realistic
 311 for reproducing experiments where the core gas flow is quiescent.

312 In our transient computations, the wavy liquid film can tend toward occluding the tube.
 313 In an experiment, such an event would form a liquid plug separated by two gas bubbles.
 314 The topological change occurring in this situation cannot be mathematically represented
 315 by our model, which implies continuous fluid layers. Thus, we apply a numerical procedure
 316 to allow our computations to continue beyond such events. For this, we level the core
 317 radius d to an arbitrary value $d_{\text{crit}}=0.1$ whenever/wherever $d \leq d_{\text{crit}}$. As a result, occluded
 318 zones are represented by a thin gas filament connecting two bubbles either side of a liquid
 319 plug (figure 3c). Although our approach allows to recover some basic features of these
 320 zones, it is a crude and invasive approximation of the actual physics. For example, every
 321 time d is reset to d_{crit} , a bit of liquid mass is lost and this can cause the unphysical
 322 reopening of liquid plugs (supplementary movies M2 and M3). We stress however, that
 323 we are not interested in studying the actual behaviour of occluded zones here. Our current

paper focusses on the events leading up to occlusion, and thus our numerical limitation of the core radius d is simply a means to continue our computations until a developed state has been reached. Nonetheless, we propose in appendix E an alternative way of representing liquid plugs in the framework of our WRIBL model, based on an additional repulsive force in the momentum equation (2.5b) that stabilizes the film surface at very small d . This approach is inspired by the representation of contact line problems with film models (Thiele *et al.* 2001), and confronting it with full-fledged plug models (Ubal *et al.* 2008; Suresh & Grotberg 2005) is an enticing prospect for future work.

2.2. Direct numerical simulation (DNS)

We have validated our model computations with selected DNS based on the full governing equations (2.1)-(2.4). These were performed with two different codes.

Transient simulations were performed with the finite volume solver Gerris (Popinet 2009), which uses the volume of fluid (Hirt & Nichols 1981) and continuum surface force (Brackbill *et al.* 1992) methods to represent the two-phase nature of the flow. We have successfully applied this code to falling liquid films in previous works (Dietze & Ruyer-Quil 2013, 2015; Dietze 2019), where further details are given. In the current work, we have used it to perform axisymmetric transient DNS on a domain spanning the wavelength Λ in streamwise direction and the tube radius R in radial direction, applying periodic streamwise boundary conditions. To allow imposing the gas pressure drop Δp_g (2.8) in this periodic setting, the streamwise momentum equations (2.1) for the liquid ($k=1$) and gas ($k=g$) were rewritten in terms of the modified pressure $\tilde{p}_k = p_k + x \Delta p_k / \Lambda$, yielding the additional source term Γ_k :

$$\Gamma_k = \frac{\Delta p_k}{\Lambda}, \quad \Delta p_1 = \Pi_\rho \Delta p_g. \quad (2.9)$$

Thanks to this source term, the governing equations can be solved with a periodicity condition on \tilde{p}_k , while the actual pressure p_k is subject to a pressure drop, allowing to control the gas flow rate. Our transient DNS were started from a flat film initial condition corresponding to the primary flow. All transient DNS were performed for case 4 in table 1, on a grid of square cells with increments $\Delta_x = \Delta_r = 2^{-7}$ in the bulk of the fluid phases and $\Delta_x = \Delta_r = 2^{-8}$ around the liquid-gas interface. The time step Δ_t was dynamically adapted so that $w^* \Delta_t / \Delta_x \leq 0.8$ in each cell, whereby w^* denotes the magnitude of the local dimensional velocity. We have verified that our simulations are grid independent. Results of our transient DNS are presented in appendix A, where they are used to validate our model computations.

The second DNS code allows to construct travelling-wave solutions of (2.1)-(2.4) based on a pseudo-spectral approach, which we have integrated into the continuation software AUTO07P (Doedel 2008). This has allowed us to verify our numerical continuation results obtained with the WRIBL model (see panel 5d). In these travelling-wave DNS, the gas phase is not accounted for, i.e. $\Pi_\mu = \Pi_\rho = 0$, and thus we have only applied them to case 3, where the effect of the gas is negligible. The underlying numerical procedure is detailed in appendix B.

2.3. Linear stability analysis

Linearizing the WRIBL model (2.5) around the uniform base state $\{d, q_k\} = \{d_0, q_{k0}\}$ and assuming a small-amplitude perturbation $\{d', q'_k\}$:

$$\begin{aligned} d(x, t) &= d_0 + d'(x, t) = d_0 + \hat{d} \exp[i(\alpha x - \omega t)] \\ q_k(x, t) &= q_{k0} + q'_k(x, t) = q_{k0} + \hat{q}_k \exp[i(\alpha x - \omega t)], \end{aligned} \quad (2.10)$$

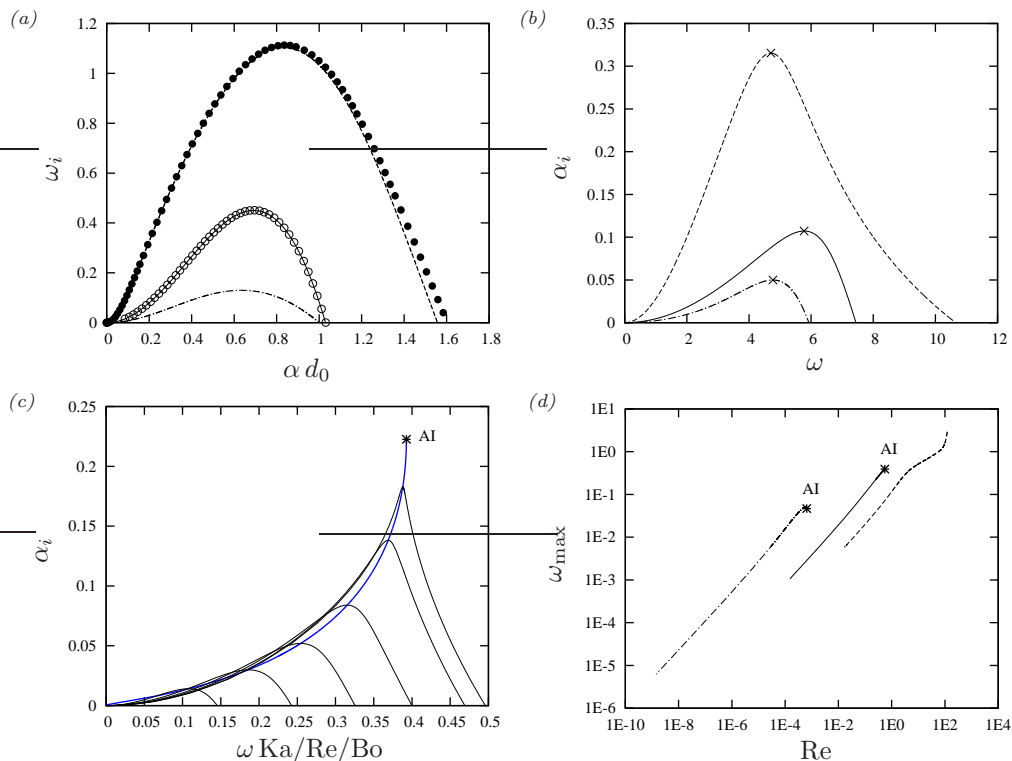


FIGURE 2. Linear instability predictions for three cases from table 1: case 1 (dot-dashed lines, diamonds); case 3 (solid lines, open circles); case 4 (dashed lines, filled circles). The core fluid is subject to an aerostatic pressure gradient $\Psi=1$. Lines correspond to the model dispersion relation (2.11). (a) Temporal growth: $\alpha \in \mathbb{R}$, $\omega = \omega_r + i\omega_i$ in (2.10). Symbols correspond to Orr-Sommerfeld solution, following the work of Hickox (1971); (b) spatial growth: $\omega \in \mathbb{R}$, $\alpha = \alpha_r + i\alpha_i$ in (2.10). Crosses highlight maximal spatial growth; (c) dispersion curves under increasing $Re \in [0.1, 0.54]$. Blue line traces maximum growth rate $\alpha_i(\omega_{\max})$; (d) most amplified angular velocity ω_{\max} versus Re . Asterisks mark absolute linear instability threshold (AI).

366 yields the complex dispersion relation:

$$\begin{aligned}
 \text{DR}(\omega, \alpha) = & 2\pi d_0 \omega \{ \varepsilon_{jl} C_{jl} + \varepsilon_{jg} \Pi_\mu C_{jg} \} + \alpha \{ \partial_d C_{jl} q_{j0} - \Pi_\mu \partial_d C_{jg} q_{j0} \} \\
 & - 2\pi d_0 \alpha^2 M_j \varepsilon_{jl} - \alpha^3 L_j q_{j0} - i \text{ReWe} \{ \alpha^2 / d_0^2 - \alpha^4 \} \\
 & + i \text{Re} \{ 2\pi d_0 [\omega^2 (S_g - Sl) + \omega \alpha (F_{jl} q_{j0} - F_{jg} q_{j0})] - \alpha^2 G_{jk} \},
 \end{aligned} \tag{2.11}$$

367 where j and k are to be permuted over the phase indicators l and g , ω designates the
 368 (complex) wave frequency, α the (complex) wave number, $\varepsilon_{ll} = \varepsilon_{gg} = -1$, and $\varepsilon_{lg} = \varepsilon_{gl} = 1$.

369 A temporal stability analysis assumes that waves grow self-similarly in their reference
 370 frame. This description implies $\alpha \in \mathbb{R}$ and $\omega = \omega_r + i\omega_i$, where the temporal growth rate
 371 ω_i is obtained by solving $\text{DR}(\omega, \alpha) = 0$. In panel 2a, we have plotted the thus obtained
 372 dispersion curve $\omega_i(\alpha)$ of the temporal growth rate for cases 1, 3 and 4 from table 1.
 373 Lines correspond to the model dispersion relation (2.11), and symbols correspond to
 374 our own numerical solutions of the Orr-Sommerfeld equations, following the work of
 375 Hickox (1971). Agreement between the two data sets is good. Thus, our model is able to
 376 accurately represent the linear wave selection.

377 In a spatially-evolving film, it is more representative to consider the spatial growth rate

378 α_i . We thus solve $\text{DR}(\omega, \alpha)=0$ for $\alpha_i(\omega)$, by assuming $\omega \in \mathbb{R}$ and $\alpha = \alpha_r + i \alpha_i$. In panel
 379 2b, we have plotted the thus obtained growth rate dispersion curves $\alpha_i(\omega)$ for the three
 380 cases from panel 2a. Crosses mark the point of maximal growth rate and we denote ω_{\max}
 381 the associated most-amplified angular velocity.

382 In section 3.2, we will characterize occlusion by determining the limit of travelling-
 383 wave solutions through numerical continuation. This limit is very sensitive to the wave
 384 frequency f . Thus we focus on the spatially most-amplified waves, which are most likely
 385 to emerge from linear wave selection in an experiment. For this, we impose the linearly
 386 most-amplified frequency $f_{\max} = 2\pi/\omega_{\max}$ in our continuation runs.

387 To determine f_{\max} , which changes with the control parameters varied in these runs,
 388 our continuation code was augmented to additionally solve for ω_{\max} subject to:

$$\text{DR}(\omega_{\max}, \alpha) = 0, \quad \partial_{\omega} \alpha_i|_{\omega=\omega_{\max}} = 0, \quad (2.12)$$

389 where $\partial_{\omega} \alpha_i$ is obtained from $\partial_{\omega} \text{DR} = 0$. In a given continuation run, the linear stability
 390 problem (2.12) is solved for the primary flow $\{q_{10}, q_{g0}\} = \{\bar{q}_1, \bar{q}_g\}$, which is fixed by the
 391 mean flow rates \bar{q}_1 and \bar{q}_g of the current travelling wave solution.

392 As shown by Camassa *et al.* (2014), the annular falling liquid film can be subject to
 393 absolute instability. Thus, we have checked for the absolute instability threshold (AI) in
 394 all our continuation runs. In the context of our spatial stability analysis, where $\omega \in \mathbb{R}$, the
 395 AI threshold bounds the solutions of (2.12) in terms of the varied control parameter, e.g.
 396 Re , because the maximum growth rate $\alpha_i(\omega_{\max})$ diverges there. For example, panel 2c
 397 represents dispersion curves $\alpha_i(\omega)$ for case 3 at different values of Re , increased toward
 398 the AI threshold. The latter is marked by an asterisk on the blue curve, which traces
 399 the locus of the spatial growth rate maximum $\alpha_i(\omega_{\max})$. We point out that ω has been
 400 rescaled in panel 2c.

401 Panel 2d represents how ω_{\max} changes with Re for the three cases from panel 2b. These
 402 curves allow to discern the AI threshold (marked by asterisks) in terms of Re . For case 4
 403 (dashed curve), we have truncated our solution at $\text{Re}=100$, beyond which our nonlinear
 404 model predictions are no longer reliable. The AI threshold lies beyond this point but, as
 405 we will see, the occlusion bound Re_{\max} lies well within the represented range (panel 6a).

406 In our current study, we focus on regimes where $\text{Bo} \geq 1$. In this case, the AI threshold is
 407 always situated beyond the limit of nonlinear travelling-wave solutions and thus it does
 408 not affect the occlusion bound. However, we will demonstrate that neglecting certain
 409 physical effects in the mathematical description, such as axial viscous diffusion (panel
 410 9b) or inertia (panel 12a), can change this.

411 3. Results and discussion

412 In subsections 3.1 and 3.2, we reproduce numerically the visualization experiments
 413 of Camassa *et al.* (2014) and demonstrate that the occlusion of a narrow tube by a
 414 wavy falling liquid film is caused by surface waves that do not possess a finite-amplitude
 415 travelling state. Depending on how these waves emerge in a spatially evolving film,
 416 either directly from linear instability (scenario I), or subsequent nonlinear dynamics
 417 (scenario II), different occlusion scenarios are possible. In subsection 3.2, we determine
 418 the bounds of these two scenarios based on the numerical continuation of travelling-
 419 wave solutions with our model (2.5). We obtain an upper conservative bound Re_{\max} ,
 420 above which occlusion in a naturally evolving film is certain, and a lower conservative
 421 bound Re_0 , below which occlusion is impossible. These bounds delimit a regime of
 422 conditional occlusion, $\text{Re}_0 < \text{Re} < \text{Re}_{\max}$, where occlusion is theoretically possible but does
 423 not necessarily occur in a real system.

Case	ρ_l (kg/m ³)	μ_l (Pas)	σ (mN/m)	R^* (mm)	Ka (-)	Π_ρ (-)	Π_μ (-)
1	970	12.9	21.5	5.0	3.3×10^{-3}	1.2×10^{-3}	1.4×10^{-6}
2	1260.7	1.049	64.0	4.765	0.30	0.95×10^{-3}	1.7×10^{-5}
3	1223.9	0.167	65.0	3.175	3.53	0.98×10^{-3}	1.1×10^{-4}
4	900	0.0045	20.0	1.5	121.4	1.3×10^{-3}	4.0×10^{-3}

Case	Re_{\max} (-)	Fr (-)	We (-)	Bo (-)	La (-)	Ca (-)	figures
1	1.91×10^{-4}	2.7×10^{-3}	8.4×10^{-5}	11.06	6.3×10^{-4}	0.37	3-5,9,11
2	0.038	0.040	7.1×10^{-3}	4.39	0.35	0.142	5,15
3	0.39	0.063	7.3×10^{-3}	1.86	9.1	0.028	5,9,15,16,18
4	18.9	0.42	0.18	0.993	1.3×10^3	0.012	6,9,12-14,17-19

TABLE 1. Representative parameters for our computations. Liquid properties correspond to a [high-viscosity silicone oil](#) (case 1), glycerol-water mixtures concentrated at 99 % and 89 % by mass (cases 2 and 3), and a low-viscosity silicone oil (case 4), while the core fluid is air with $\mu_g=1.8 \cdot 10^{-5}$ Pas and $\rho_g=1.2$ kg/m³. Case 1 corresponds to figure 3a in Camassa *et al.* (2014), and cases 2 and 3 correspond to experimental runs 20 and 13 in Dao & Balakotaiah (2000). The dimensionless groups are $Bo=\rho_l g \mathcal{L}^2/\sigma$, $Ca=\mu_l \mathcal{U}/\sigma$, $Re=\rho_l \mathcal{U} \mathcal{L}/\mu_l$, $Ka=\sigma \rho_l^{-1} g^{-1/3} \mu_l^{-4/3}$, $La=\sigma \rho_l \mathcal{L}/\mu_l^2$, $We=\rho_l \mathcal{U}^2 \mathcal{L}/\sigma$, and $Fr=\mathcal{U}/\sqrt{g \mathcal{L}}$, where $\mathcal{L}=R^*$ and $\mathcal{U}=q_{10}^*/\pi/\mathcal{L}^2$, q_{10}^* designating the dimensional nominal liquid flow rate. Re_{\max} is the upper conservative occlusion bound (see e.g. panels 5a and 5b).

424 In subsection 3.7, we demonstrate occlusion scenarios I and II, which are associated
425 with the regimes of certain ($Re > Re_{\max}$) and conditional occlusion ($Re_0 < Re < Re_{\max}$), by
426 reproducing two of the experiments in Dao & Balakotaiah (2000) with our own spatio-
427 temporal computations. Before that, in subsections 3.3 to 3.6, we establish how different
428 physical effects, i.e. gravity, axial viscous diffusion, inertia, and the core gas flow, affect the
429 upper conservative bound Re_{\max} , which delimits these two regimes. Except for section 3.6,
430 where we will vary the gas Reynolds number Re_g , our computations have been performed
431 for an aerostatic pressure drop, i.e. $\Psi=1$. This is most representative of experiments in a
432 quiescent gas.

433 Parameters for our computations are varied around the four cases listed in table 1,
434 which represent real liquids and plausible values of the tube radius. Case 1 corresponds to
435 figure 3a in Camassa *et al.* (2014), where the working liquid was a [high-viscosity silicone](#)
436 [oil](#). Cases 2 and 3 correspond to experimental runs 20 and 13 in Dao & Balakotaiah
437 (2000), where glycerol-water mixtures concentrated at 99 % and 89 % by mass were
438 used. Finally, case 4 concerns a liquid film of low-viscosity silicone oil. The four cases
439 cover a considerable range of the Laplace number $La=\sigma \rho_l R^*/\mu_l^2$, which relates capillarity
440 to viscous drag, and the Reynolds number, which we have quantified with Re_{\max} . We see
441 that inertia, which drives the Kapitza instability, is significant for case 4. For this case,
442 which is the most challenging, we have validated our model computations with transient
443 DNS in appendix A ([comparisons with travelling-wave DNS, for case 3, are reported in](#)
444 [panel 5d](#)).

3.1. Nature of the surface waves that cause occlusion

445 Camassa *et al.* (2014) performed occlusion experiments in an $R^*=0.5$ mm and $L^*=400$
446 mm transparent tube using [high-viscosity silicone oil](#) (case 1 in table 1). In their figure 3,
447 the authors produce photographs of the wavy falling liquid film at different Re beyond the
448

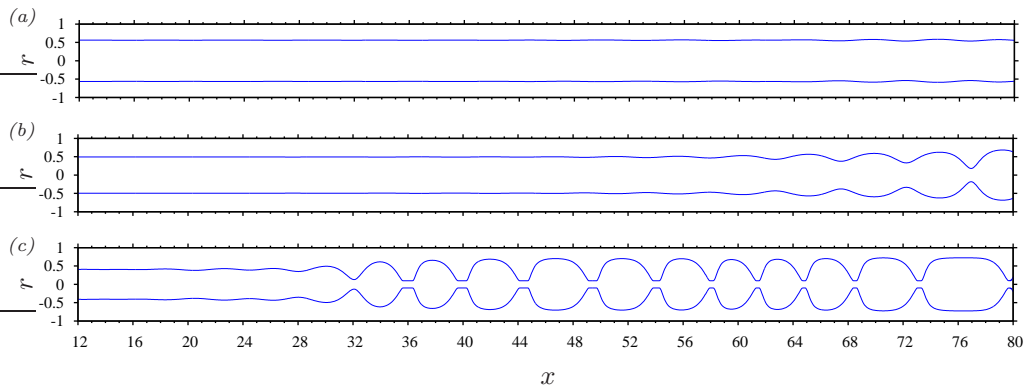


FIGURE 3. Spatio-temporal computations of the experiments in panels 3a, 3b, and 3c of Camassa *et al.* (2014), which were performed in an $L^* = 400$ mm tube. Parameters correspond to case 1 in table 1. Computations were performed with our model (2.5) using inlet/outlet conditions and the noisy inlet perturbation (2.6), where we have set $\epsilon_1 = 0$ and adjusted ϵ_2 to match the experimental wave growth. (a) $Re = 2.3 \times 10^{-4}$, $q_{10}^* = 4.8 \times 10^{-2}$ cm³/s, $\epsilon_2 = 0.0002$; (b) $Re = 3.2 \times 10^{-4}$, $q_{10}^* = 6.7 \times 10^{-2}$ cm³/s, $\epsilon_2 = 0.00005$; (c) $Re = 4.5 \times 10^{-4}$, $q_{10}^* = 9.4 \times 10^{-2}$ cm³/s, $\epsilon_2 = 0.0001$.

449 experimental occlusion threshold, allowing to discern the nature of the surface waves that
 450 cause occlusion. We have reproduced three of these experiments with spatio-temporal
 451 computations based on our model (2.5) on a long domain using inlet/outlet conditions
 452 (see section 2.1). **Experimental noise was mimicked through the noisy inlet perturbation**
 453 **(2.6), where we have set $\epsilon_1 = 0$, and tuned ϵ_2 to match the spatial evolution of surface**
 454 **waves in the experiments (when decreasing/increasing ϵ_2 , the region of linear growth of surface**
 455 **waves is stretched/compressed in streamwise direction and this shifts the emergence of**
 456 **nonlinear effects, such as occlusion, downstream/upstream).** Figure 3 shows snapshots
 457 of these computations, which are to be directly compared to panels 3a, 3b, and 3c in
 458 Camassa *et al.* (2014).

459 Agreement with the experimental snapshots is good. In particular, the wavelength of
 460 the four distinct surface waves at the tube outlet in panel 3b is predicted accurately
 461 by our computations. Also, the number of gas bubbles (eleven) in panel 3c, which
 462 result from successive occlusion events, agrees with the experiment. Panel 3c and the
 463 supplementary movie M1 allow to discern the actual mechanics of occlusion. Surface
 464 waves in the upstream portion of the tube grow spatially until their crests reach the tube
 465 axis, whereupon individual bubbles of the gas core are pinched off. Our model accurately
 466 predicts the length scale of the pinch-off process in comparison with the experiment. We
 467 stress that panel 3c is a snapshot and that the occlusion point shifts up and down the tube
 468 intermittently as a result of the noisy wave spectrum imposed through the inlet condition.
 469 **These results show that our model captures accurately the wave dynamics leading up to**
 470 **occlusion, and this is the focus of our current study. However, the physics of the liquid**
 471 **plugs resulting from occlusion is captured only very crudely by the numerical core radius**
 472 **limitation introduced in section 2.1. For example, the shape of the gas bubbles in panel**
 473 **3c is quite different from that in the experiment and their length evolves as they travel**
 474 **downstream (see also supplementary movie M1). First results reported in appendix E**
 475 **suggest that these shortcomings can be alleviated with our improved WRIBL model. But,**
 476 **the exact shape of liquid plugs can never be fully captured in the context of lubrication**
 477 **theory, as the film surface slope diverges at their edges.**

478 We focus now on panel 3a, where Re is closest to the experimental occlusion threshold.

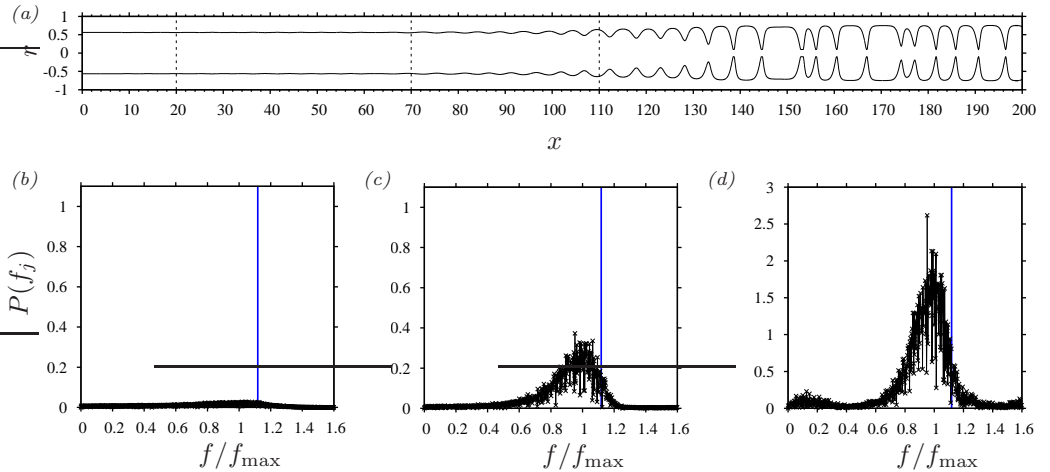


FIGURE 4. Nature of the prevailing surface waves that cause occlusion. Spatio-temporal computation reproducing the second version of the experiment in panel 3a of Camassa *et al.* (2014), which was performed in a longer $L^*=1$ m tube: case 1 in table 1, $\text{Re}=2.3 \times 10^{-4}$. (a) Snapshot of the computed film profile, showing individual surface waves that cause occlusion in the region $x \geq 130$; (b-d) frequency spectra at different streamwise locations leading up to the occlusion region (marked by dashed lines in panel a): (b) $x=20$; (c) $x=70$; (d) $x=110$. Vertical blue lines at $f/f_{\max}=1.12$ mark limit of travelling wave solutions determined by numerical continuation (see panel 6b). f_{\max} designates spatially most amplified frequency of linear waves.

479 For this case, Camassa *et al.* (2014) observed occlusion only after having switched to a
 480 longer $L^*=1$ m tube. Because of the small spatial growth rate, distinguishable surface
 481 waves emerged only very close to the outlet of the shorter $L^*=400$ mm tube, and their
 482 amplitude was insufficient to cause occlusion there. Our computation in panel 3a exhibits
 483 the same behaviour.

484 We have also reproduced numerically the experiment in the $L^*=1$ m tube and a
 485 snapshot of our computation is represented in panel 4a. It confirms that occlusion does
 486 indeed occur, in the region $x \geq 130$. **Occlusion results from unbounded spatial growth**
 487 **of the prevailing surface waves, and panels 4b to 4d show how the latter emerge from**
 488 **the noisy inlet condition. In these panels, we have represented the single-sided amplitude**
 489 **spectrum $P(f_j)$ of the discrete Fourier transform $F(f_j)$ applied to core radius time series**
 490 **$d(t_k)$ recorded at different streamwise positions x (marked by dashed lines in panel 4a),**
 491 **leading up to the occlusion region:**

$$P(f_j) = (2/N) F(f_j) \forall j \leq N/2 + 1, \quad F(f_j) = \sum_{k=0}^N d(t_k) \exp(i 2\pi j/N k), \quad (3.1)$$

492 where $N=1.8 \cdot 10^6$ is the number of (equidistant) sampling points t_k with which we have
 493 recorded the time series $d(t_k)$ over a duration $T=9.1 \cdot 10^4$, and $f_j=(j/N)/T$ are the
 494 frequencies of the discrete spectrum. At the most downstream location (panel 4d), the
 495 spectrum is organized around the spatially most amplified frequency of linear waves f_{\max}
 496 in the form of a quite narrow peak. This peak lies beyond the limit $f/f_{\max}=1.12$ for the
 497 existence of travelling-wave solutions at the considered Reynolds number $\text{Re}=2.3 \times 10^{-4}$,
 498 which is highlighted by vertical blue lines in panels 4b, 4c, and 4d. This limit has been
 499 determined by numerical continuation of travelling-wave solutions, which we will discuss
 500 in the next subsection (it is marked by an asterisk in panel 5b). We will see that higher

501 frequency (shorter) waves are safe from and lower frequency (longer) waves are prone to
 502 occlusion.

503 By way of numerical continuation, Camassa *et al.* (2014) were the first to show that the
 504 existence of travelling-wave solutions is bounded. By increasing Re at fixed wavelength,
 505 the authors found a limit point beyond which travelling-wave solutions cease to exist.
 506 They conjectured that the loss of such solutions signals occlusion in an actual experiment.
 507 However, the authors cautioned that further work was needed to verify this conjecture.
 508 This work was initiated by Camassa *et al.* (2016), but their model did not account for
 509 axial viscous diffusion. Our computations in figures 3 and 4 provide further validation, by
 510 taking into account this effect, which greatly improves agreement of our model predictions
 511 with the experiments of Camassa *et al.* (2014), as a result of the high viscosity of
 512 the working liquid. For example, when running the computation in panel 4a without
 513 axial viscous diffusion, we did not observe any occlusion over the entire experimental
 514 tube length (see figure 21 in appendix D), which is in qualitative contradiction to the
 515 experiments. Also, we will show in subsection 3.4 that neglecting axial viscous diffusion
 516 increases Re_{\max} by 74% for this liquid (panel 9a), moving it far beyond the experimental
 517 occlusion limit, as quantified in terms of Re .

518 Figure 4 proves that the occlusion of a narrow tube by a wavy falling liquid film is
 519 caused by surface waves that lie beyond the limit of travelling-wave solutions. Thus,
 520 occlusion can be characterized based on the existence span of such solutions and we
 521 proceed to this in the following subsection.

522 3.2. Travelling waves: regimes of certain, conditional, and impossible occlusion

523 The frequency of travelling waves determines their amplitude, which is well known
 524 for planar falling liquid films (Nosoko *et al.* 1996) and also holds in our cylindrical
 525 configuration. At a given value of Re , the smaller the wave frequency, the greater the wave
 526 amplitude. Consequently, low-frequency travelling waves are more prone to occlusion than
 527 high-frequency waves. This effect was demonstrated by Camassa *et al.* (2016) and Ding
 528 *et al.* (2019) with a first-order asymptotic model and a lubrication model, respectively.
 529 Using our model (2.5), we quantify it for the real liquids studied here (cases 1-4 in table
 530 1), which require a more complicated modelling approach.

531 Panel 5a represents curves of travelling-wave solutions for case 1 in terms of the minimal
 532 core radius d_{\min} , as obtained by varying the liquid Reynolds number Re . On each curve,
 533 we have fixed the wave frequency f to a certain fraction f/f_{\max} of the spatially most
 534 amplified frequency f_{\max} , which we determine through the approach outlined in section
 535 2.3. All curves display a limit point in terms of Re , beyond which there are no travelling-
 536 wave solutions. The existence of such a limit point was discovered by Camassa *et al.*
 537 (2014), who imposed a constant wavelength in their continuation. This wavelength was
 538 too long compared to their experiments, whereas we see here that accounting for the
 539 correct wavelength/frequency is quite important. Indeed, the limit point of the curves in
 540 panel 5a varies greatly with f/f_{\max} . The lower the wave frequency, the smaller the limit
 541 value of Re , the more danger of occlusion.

542 We now introduce the upper conservative occlusion bound Re_{\max} , which corresponds to
 543 the limit point (LP) of the solid line representing the spatially most amplified travelling
 544 waves, i.e. $f/f_{\max}=1$. For $Re > Re_{\max}$, the linearly most amplified surface waves, which
 545 are most likely to emerge in an experiment, do not possess travelling states and occlusion
 546 is certain to occur in a naturally evolving film. The experiment of Camassa *et al.* (2014),
 547 which we have reproduced numerically in figure 4, corresponds to this regime. Occlusion
 548 in this case occurs through scenario I, which we will discuss further in section 3.7 based
 549 on spatio-temporal computations.

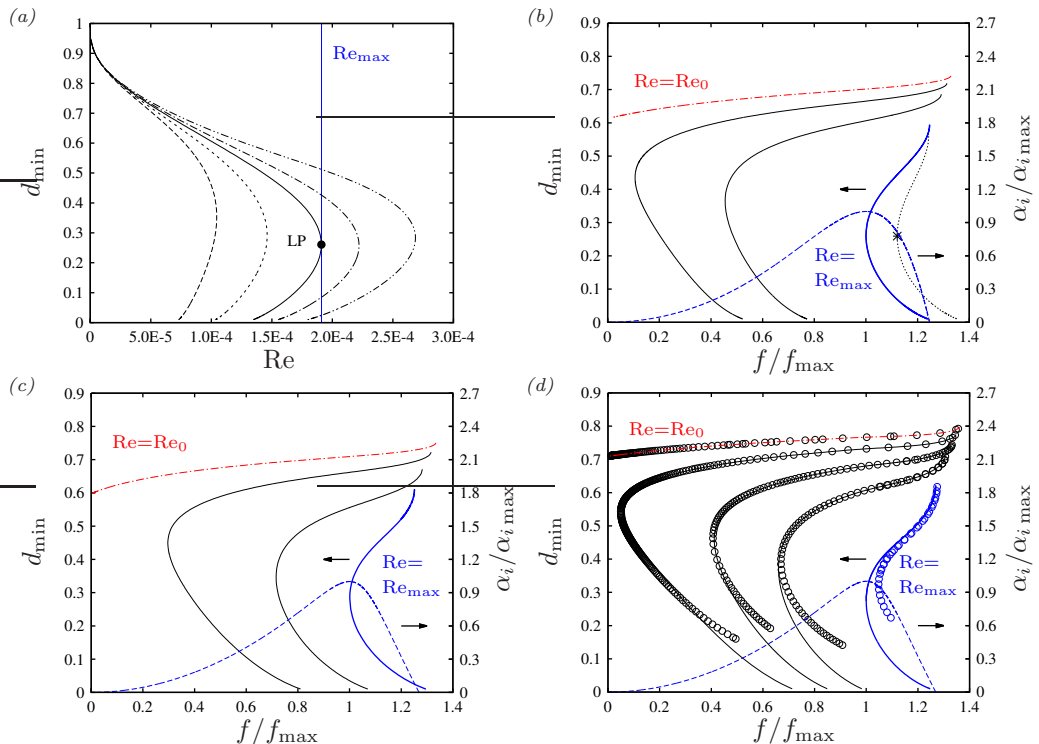


FIGURE 5. Limits of travelling-wave solutions obtained from numerical continuation with our model (2.5). Cases 1 (panels *a*, *b*), 2 (panel *c*), and 3 (panel *d*) in table 1. (*a*) Continuation of Re at wave frequency $f/f_{\max}=0.5$ (long dashes), 0.8 (short dashes), 1 (solid), 1.1 (dot-dashed), and 1.2 (dot-dot-dashed). Vertical blue line marks limit point (LP) for spatially most amplified linear waves, where $f=f_{\max}$ and $\text{Re}=\text{Re}_{\max}$; (*b-d*) frequency dependence at $\text{Re}=\text{const}$. Dashed blue: linear spatial growth rate α_i at $\text{Re}=\text{Re}_{\max}$ (right abscissae), other: travelling-wave solutions at $\text{Re}=\text{const}$ (left abscissae). (*b*) Case 1: $\text{Re}=\text{Re}_0=6 \times 10^{-5}$ (dot-dashed red), $\text{Re}=7.5 \times 10^{-5}$, 1×10^{-4} (thin solid), $\text{Re}=\text{Re}_{\max}=1.91 \times 10^{-4}$ (thick solid blue), and $\text{Re}=2.3 \times 10^{-4}$ (dotted with asterisk); (*c*) case 2: $\text{Re}=\text{Re}_0=0.012$ (dot-dashed red), $\text{Re}=0.016$, 0.025 (thin solid), and $\text{Re}=\text{Re}_{\max}=0.038$ (thick solid); (*d*) case 3: $\text{Re}=\text{Re}_0=0.075$ (dot-dashed red), $\text{Re}=0.1$, 0.14 , 0.2 (thin solid), and $\text{Re}=\text{Re}_{\max}=0.393$ (thick solid). Open circles correspond to data obtained with our own travelling-wave DNS (see section 2.2).

550 Panel 5b explains the meaning of the upper occlusion bound Re_{\max} in a different
 551 way, by illustrating the effect of the wave frequency f at fixed Re . The dashed blue
 552 line represents the linear spatial growth rate α_i at $\text{Re}=\text{Re}_{\max}$ (right abscissa), while
 553 all other curves represent travelling-wave solutions (left abscissa) at different Re . These
 554 curves all display a limit point in terms of f . The dotted line marked by an asterisk
 555 corresponds to the experiment of Camassa *et al.* (2014) numerically reproduced in figure
 556 4, where $\text{Re}=2.3 \times 10^{-4}$. The thick blue solid line corresponds to the upper occlusion
 557 bound $\text{Re}=\text{Re}_{\max}=1.9 \times 10^{-4}$ and its limit point thus coincides with the maximum of
 558 the growth rate dispersion curve $\alpha_i(f)$. We stress that determining Re_{\max} requires
 559 simultaneously computing the most amplified wave frequency f_{\max} in our numerical
 560 continuations, as described in section 2.3. This had not been attempted in the previous
 561 studies of Camassa *et al.* (2014) and Ding *et al.* (2019).

562 Reducing Re below Re_{\max} moves the limit point of travelling-wave solutions to lower
 563 values of f . Thus, the occlusion range is increasingly confined to (very long) waves of

564 very low frequency, until it vanishes completely at $\text{Re}=\text{Re}_0$ (red dot-dashed curve in panel
 565 5b). This limit, the existence of which was discovered by Ding *et al.* (2019), constitutes
 566 a lower conservative occlusion bound. When $\text{Re}<\text{Re}_0$, occlusion is impossible, no matter
 567 how long the waves. In a real system, it is conceivable that wave coalescence events
 568 can produce local overshoots leading to occlusion even when $\text{Re}<\text{Re}_0$. However, we have
 569 not observed this in our computations of spatially evolving films (see panels 16b and
 570 17c). The value Re_0 being very low for all studied liquids, inertia is weak and significant
 571 overshoots are unlikely.

572 Based on the conservative occlusion bounds Re_0 and Re_{max} , we delimit a region of
 573 conditional occlusion, $\text{Re}_0<\text{Re}<\text{Re}_{\text{max}}$ (between the red dot-dashed and thick solid blue
 574 lines in panel 5b), where occlusion is theoretically possible, for long enough waves, but
 575 does not necessarily occur in a real system. That depends on whether the required waves
 576 actually develop in a spatially evolving film. And, in particular, whether the tube is
 577 long enough to accommodate the nonlinear wave dynamics required to produce them. In
 578 section 3.7, we will demonstrate that occlusion in this regime occurs through scenario II,
 579 i.e. wave coarsening triggered by secondary instability, which shifts surface waves down
 580 the ascending branch of the dispersion curve toward increasingly low frequencies.

581 In panel 5a, the limit point LP is a turning point, where two solution branches meet.
 582 As suggested by Camassa *et al.* (2014), we have checked their stability using transient
 583 periodic simulations with imposed Ψ started from selected travelling-wave solutions. In
 584 these computations, numerical noise is responsible for perturbing the flow. A full-fledged
 585 formal stability analysis, such as the one performed by Camassa *et al.* (2016) based on
 586 the first-order model of Camassa *et al.* (2014), is outside the scope of our current study.
 587 We find that the lower solution branch is entirely unstable. As this branch does not
 588 connect to the flat-film primary flow $d_{\text{min}}=d_{\text{max}}=1$, the solutions thereon are thus highly
 589 unlikely in an experiment. Conversely, the upper branch is stable, at least w.r.t. periodic
 590 perturbations. However, wave trains of high-frequency travelling waves on falling liquid
 591 films are subject to secondary subharmonic and sideband instabilities that rely on wave
 592 interaction and lead to coalescence events (Liu & Gollub 1993). We have found that this
 593 triggers occlusion scenario II, which we will demonstrate in §3.7. Finally, when starting
 594 a periodic transient computation from a flat-film initial condition beyond the limit of
 595 travelling-wave solutions, the outcome is indeed occlusion, which we have checked (and
 596 validated with transient DNS) in appendix A (see panels 19a and 19b).

597 Panels 5c (case 2), 5d (case 3), and figure 6 (case 4) report the occlusion bounds
 598 Re_{max} and Re_0 for the other three cases from table 1. In panel 5d, we have represented
 599 with open circles additional results obtained with our own travelling-wave DNS (see
 600 section 2.2), evidencing gratifying agreement with our WRIBL model predictions. Overall
 601 tendencies in these graphs are the same as for case 1. For case 4 (low-viscosity silicone
 602 oil), where the Kapitza instability is relevant, there is an additional feature. In panel 6a,
 603 the continuation curves of $d_{\text{min}}(\text{Re}, f=\text{const})$ at high frequencies, e.g. the dot-dot-dashed
 604 curve at $f/f_{\text{max}}=1.2$, exhibit two lobes that are each associated with a limit point. Wave
 605 profiles corresponding to these highlighted points LP1 and LP2 are represented in panel
 606 6c. We see that the main wave hump is preceded by a small precursory ripple. Such so-
 607 called capillary ripples can produce multiplicity of solutions in falling liquid films, when
 608 they are close enough to interact with the following wave hump (Kalliadasis *et al.* 2012).
 609 By contrast, the dashed curves in panel 6a, which pertain to low-frequency waves, each
 610 display only a single limit point (LP). Panels 6d and 6e show the corresponding wave
 611 profiles at those points. We see in panels 6c, 6d, and 6e that lower wave frequencies are
 612 associated with longer wavelengths, which we have implicitly assumed up until now.

613 Finally, panel 6f represents the wave profile corresponding to the limit point (LP)

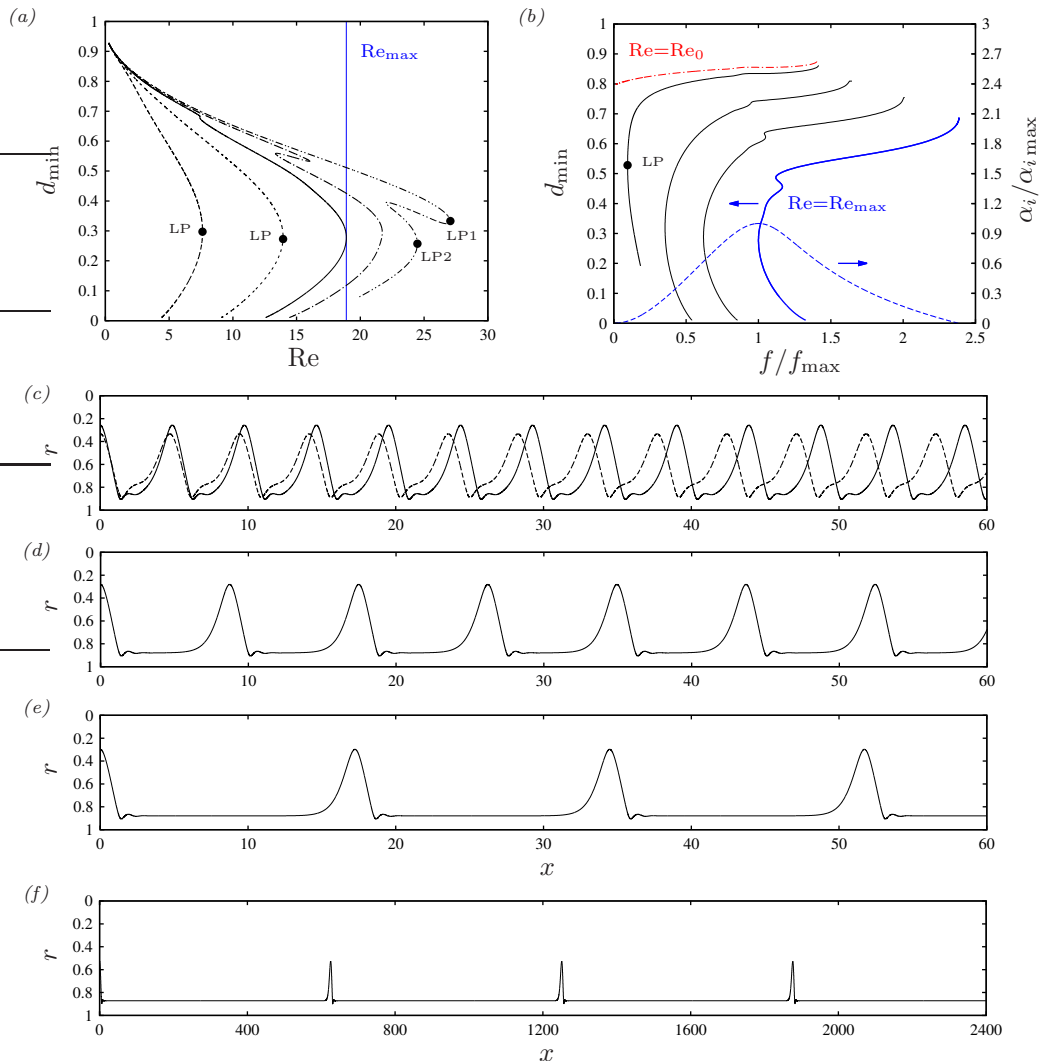


FIGURE 6. Limits of travelling-wave solutions for case 4 in table 1. (a) Continuation of Re at constant wave frequency $f/f_{\max}=0.5$ (long dashes), 0.8 (short dashes), 1 (solid), 1.1 (dot-dashed), and 1.2 (dot-dot-dashed); (b) frequency dependence at $Re=\text{const}$. Dashed: linear spatial growth rate α_i at $Re=Re_{\max}=18.9$ (right abscissa); other: travelling-wave solutions (left abscissa) at $Re=Re_0=1.5$ (dot-dashed red), $Re=2, 5, 10$ (thin solid), and $Re=Re_{\max}$ (thick blue); (c-e) film profiles for LPs marked by filled circles in panel a; (c) $f=1.2f_{\max}$. Solid: LP1; dashed: LP2; (d) $f=0.8f_{\max}$; (e) $f=0.5f_{\max}$; (f) profile for marked LP in panel b.

614 marked by a filled circle on the $Re=2$ curve in panel 6b. This curve lies in the region of
 615 conditional occlusion, $Re_0 < Re < Re_{\max}$ ($Re_0=1.5$, $Re_{\max}=18.9$). However, based on the
 616 wavelength of the waves in panel 6f, which span about 600 times the tube radius, it
 617 becomes clear that quite particular conditions can be required to cause occlusion in this
 618 regime. This underlines the conservative nature of the lower occlusion bound Re_0 .

619 In summary, due to the frequency dependence of travelling-wave solutions demon-
 620 strated in panels 5b, 5c, 5d, and 6b, three characteristic regimes can be delimited: (i)
 621 impossible occlusion, when $Re < Re_0$, (ii) conditional occlusion, when $Re_0 < Re < Re_{\max}$,

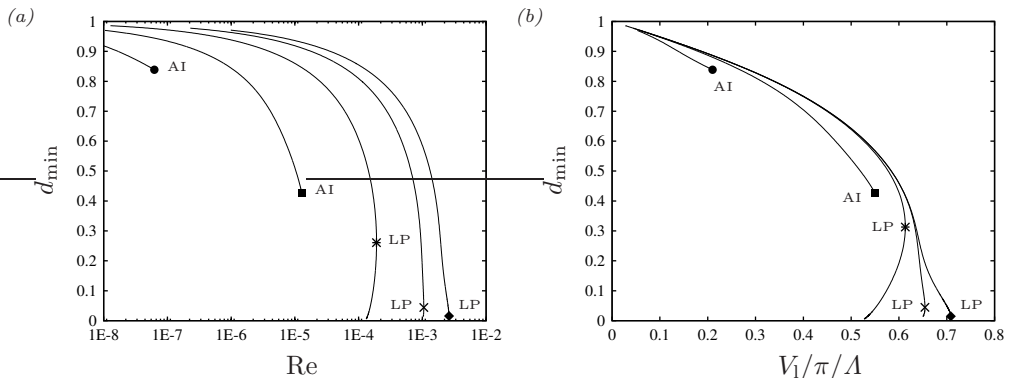


FIGURE 7. Delay of occlusion by increasing the Bond number $Bo=\rho_1 g R^{*2}/\sigma$ at constant Laplace number: $La=\sigma \rho_1 R^*/\mu_1^2=6.27\times 10^{-4}$ (case 1). Travelling-wave solutions at $f=f_{\max}$. Symbols mark onset of absolute linear instability (AI) or limit points (LP). The limit points correspond to the upper occlusion bound Re_{\max} . Circles: $Bo=0.1$; squares: $Bo=1$; asterisks: $Bo=11.1$ (case 1); crosses: $Bo=50$; diamonds: $Bo=100$. (a) Minimal core radius d_{\min} versus liquid Reynolds number; (b) minimal core radius versus liquid holdup.

622 and (iii) certain occlusion, when $Re > Re_{\max}$. In section 3.7, we will characterize these
 623 regimes with spatio-temporal computations and demonstrate the associated occlusion
 624 scenarios I and II. On the other hand, the frequency dependence of travelling-wave
 625 solutions opens the possibility of using coherent inlet forcing to prevent occlusion. By
 626 forcing regular waves of sufficiently high frequency, occlusion can be avoided versus a
 627 noise-driven wave evolution. We demonstrate this idea in section 3.8 based on spatio-
 628 temporal computations. In the next sections, 3.3 to 3.6, we first proceed to establish how
 629 different physical effects, i.e. gravity, axial viscous diffusion, inertia, and the core gas
 630 flow, affect the upper conservative occlusion bound Re_{\max} .

631

3.3. Role of gravity

632

The upper occlusion bound Re_{\max} can be significantly delayed by increasing the relative
 633 strength of gravity versus capillarity. We have quantified this by varying the Bond
 634 number $Bo=\rho_1 g R^{*2}/\sigma$ over several orders of magnitude at constant Laplace number
 635 $La=6.3\times 10^{-4}$. This value of La corresponds to the [high-viscosity silicone oil](#) (case 1),
 636 where inertia is always negligible.

637

Panel 7a represents travelling-wave solutions for different values of Bo . On each curve,
 638 we have imposed the frequency f_{\max} of the most amplified spatially growing linear waves.
 639 All curves exhibit a limit value for the liquid Reynolds number Re . For $Bo \ll 1$, where
 640 the Plateau-Rayleigh instability dominates, this limit is dictated by the onset of absolute
 641 instability (AI), as discussed in panels 2c and 2d. Beyond this point, prevailing waves are
 642 no longer characterized by the most-amplified spatially growing linear waves and f_{\max}
 643 is no longer defined. The solution curves stop abruptly. Occlusion in this regime is caused
 644 by absolute instability of the primary flow. This regime is not the focus of our study.

645

We focus on $Bo \geq 1$, for which the solution curves in panel 7a are bounded by a limit
 646 point (LP), as discussed in panel 5a. This limit point marks the upper occlusion bound
 647 Re_{\max} , which increases significantly with increasing Bo , while the minimal core radius
 648 d_{\min} at LP significantly diminishes. The first observation is in line with the experiments
 649 of Dao & Balakotaiah (2000), who reported Re at the experimental occlusion onset for
 650 different liquids and tube radii but had no access to the wave dynamics. The authors also

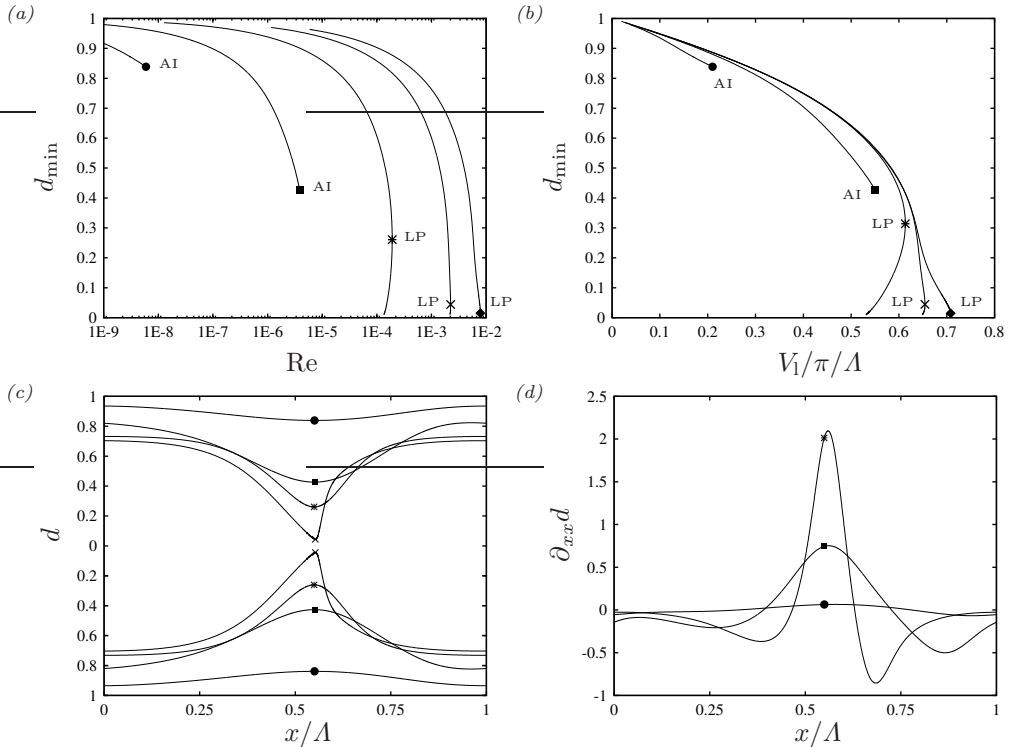


FIGURE 8. Delay of occlusion by increasing the Bond number Bo at constant Kapitza number: $Ka = \sigma \rho_1^{-1} g^{-1/3} \mu_1^{-4/3} = 3.29 \times 10^{-4}$ (case 1). This amounts to increasing the tube radius R^* while maintaining constant fluid properties. See figure 7 for symbol attributions. (a) Minimal core radius d_{\min} versus liquid Reynolds number; (b) minimal core radius versus liquid holdup; (c) surface profiles at AI and LP; (d) corresponding profiles of axial curvature $\partial_{xx}d$.

651 outlined an approach for predicting occlusion based on travelling waves, which relied on
 652 the conjecture that the wave height always reaches the tube radius as Re is increased
 653 toward the occlusion limit. Based on our results in panel 7a, this conjecture only holds
 654 when Bo is extremely large. Otherwise, travelling-wave solutions are lost well before their
 655 height attains the tube radius.

656 In panel 7b, we have replotted our results from panel 7a in terms of the liquid hold-up
 657 $V_l/\pi/\Lambda$. We see that the maximally achievable liquid hold-up increases significantly with
 658 Bo . This again is in line with the experiments of Dao & Balakotaiah (2000), who had
 659 observed that the mean film thickness \bar{h} at occlusion is significantly greater than in the
 660 gravity-free Plateau-Rayleigh configuration (Gauglitz 1988).

661 The variation of Bo in figure 7 amounts to varying the gravitational acceleration for
 662 constant liquid and tube radius. Of course, it is either very difficult (low Bo range,
 663 microgravity experiments) or impossible (high Bo range) to realize the displayed range of
 664 variation $0.1 \leq Bo \leq 100$ practically. A more practicable way to quantify the desired effect
 665 is to increase the tube radius R for a constant liquid. This amounts to increasing Bo at
 666 constant $Ka = \sigma \rho_1^{-1} g^{-1/3} \mu_1^{-4/3}$. We have performed such computations for $Ka = 3.3 \times 10^{-3}$,
 667 corresponding to the high-viscosity silicone oil (case 1). Results are represented in panels
 668 8a and 8b, and these display the same overall behaviour as figure 7.

669 The delay of Re_{\max} results from a gravity-induced streamwise distortion of surface
 670 waves, which favours variations in (stabilizing) axial interface curvature over variations in

(destabilizing) azimuthal curvature. Panel 8c illustrates this distortion, which is marked by a compression of the leading wave front and an elongation of the trailing front. The different surface profiles represented correspond to the absolute instability thresholds (AI) and limit points (LP) highlighted in panel 8a. Panel 8d represents corresponding profiles of the axial curvature $\partial_{xx}d$. The variation in (stabilizing) axial curvature $\partial_{xx}d$ around the wave crest (marked by a symbol) significantly increases in magnitude with increasing Bo. This allows to counter a larger variation in (destabilizing) azimuthal curvature, and, thus, to saturate waves of greater amplitude.

The saturation mechanism was identified by Frenkel *et al.* (1987) for pressure-driven core annular flows, where it is due to a viscous interfacial shear stress, and demonstrated experimentally for falling liquid films on cylindrical fibres by Qu  r   (1990). In both studies, the saturation took hold in the weakly-nonlinear regime, limiting waves to a very small amplitude. Thus, it was perceived as suppressing macroscopically-visible waves altogether. In our case, the mechanism takes hold in the strongly-nonlinear regime, allowing to saturate travelling waves of greater amplitude as Bo is increased.

The role of gravity is kinematic, i.e. it makes initial surface elevations travel faster than surface depressions (Dietze 2016), and this produces the distortion of wave fronts observed in panel 8c. We point out that this effect was precluded in Jensen (2000), where surface waves were constructed in the form of perfectly symmetrical unduloids.

3.4. Role of axial viscous diffusion

Axial viscous diffusion, emanating from the $\partial_{xx}u$ term in (2.1), is represented in our model (2.5) through the terms with coefficients J_j , K_j , L_j , and M_j . These terms appear when the underlying long-wave expansion is performed up to second order. This was not done in the previous modelling works of Trifonov (1992), Camassa *et al.* (2014, 2017), Zhou *et al.* (2016), Liu & Ding (2017), and Ding *et al.* (2019). So, the question is whether retaining these terms is worth the effort. We have checked this in panels 9a, 9b, and 9d, representing travelling-wave solutions for cases 1, 3, and 4. The three cases span a wide range of the capillary number $\text{Ca}=\mu_1\mathcal{U}/\sigma$, which relates viscous to capillary stresses, and which quantifies the relevance of axial viscous diffusion.

In figure 9, solid lines correspond to the full model (2.5) and dot-dashed lines to the limit $J_i=K_i=L_i=M_i=0$. Further, we distinguish two types of continuations. On the blue curves, which contain no symbols, we have fixed the wavelength $\Lambda=12.56$. On the black curves with symbols, we have imposed the spatially most amplified frequency of linear waves $f=f_{\max}$. In that case, axial viscous diffusion may affect the solution both non-linearly and linearly (via wave selection), but the latter effect is negligible for the cases considered here. By comparing the solid and dashed curves in panels 9a, 9b, and 9d, we see that axial viscous diffusion precipitates occlusion in general and Re_{\max} in particular and this effect increases with Ca.

For the high-viscosity silicone oil (panel 9a, case 1: $\text{Ca}=0.37$), accounting for axial viscous diffusion greatly reduces Re_{\max} , i.e. from $\text{Re}_{\max}=3.3\text{E-}4$ to $\text{Re}_{\max}=1.9\text{E-}4$ (compare dot-dashed and solid black lines with symbols). It is insightful to compare these values to the experimental occlusion bound, which was observed by Camassa *et al.* (2014) between $\text{Re}=1.6\text{E-}4$ and $\text{Re}=2.3\text{E-}4$ for their 1 m long tube. Linear interpolation based on their table 1 and figure 11 yields a value of $\text{Re}=2.2\text{E-}4$, which is not much greater than our Re_{\max} prediction with ($\text{Re}_{\max}=1.9\text{E-}4$) but much smaller than our prediction without axial viscous diffusion ($\text{Re}_{\max}=3.3\text{E-}4$). Interestingly, when basing the comparison on the mass-equivalent core radius $d_m=(L^{-1}\int_0^L d^2 dx)^{1/2}$, which was also measured by Camassa *et al.* (2014), our two predictions ($d_m^*=0.31$ cm versus $d_m^*=0.25$ cm) lie equally close to the

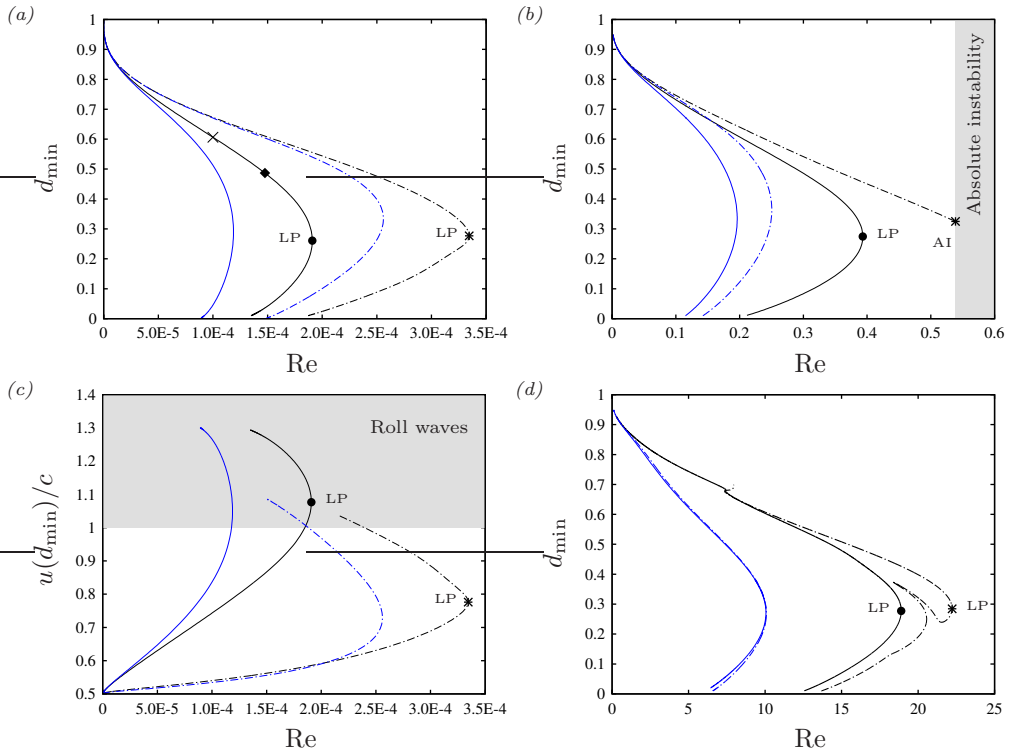


FIGURE 9. Precipitation of occlusion due to axial viscous diffusion. Cases 1, 2, and 3. Circles/asterisks mark limit points (LP) and absolute instability onset (AI). Solid lines: full model (2.5); dot-dashed lines: no axial viscous diffusion, $J_j=K_j=L_j=M_j=0$ in (2.5) and (2.11); black curves with symbols: $f=f_{\max}$; blue lines without symbols: $A=12.56$. The capillary number Ca scales the observed effect. (a, c) Case 1: $Ca=0.37$. Cross and diamond mark points used in figure 10. Panel c represents ratio of interfacial fluid velocity $u(d_{\min})$ to wave speed c . Grey region marks existence of roll waves $u(d_{\min}) > c$; (b) case 3: $Ca=0.028$. In the grey region, the primary flow is absolutely unstable (AI); (d) case 4: $Ca=0.012$.

719 experimental value $d_m^*=0.28$ cm. This explains why Camassa *et al.* (2014, 2016) observed
 720 good agreement in terms of this parameter, although their model did not account for axial
 721 viscous diffusion. Finally, we point out that the corresponding values of the primary-flow
 722 core radius d_0 , which is more representative of the flat film portion in the upper part
 723 of the experimental tube, are $d_0^*=0.29$ cm with and $d_0^*=0.24$ cm without axial viscous
 724 diffusion.

725 For case 3 (panel 9b, $Ca=0.028$), which corresponds to experimental run 13 in Dao
 726 & Balakotaiah (2000), axial viscous diffusion dictates even the nature of the occlusion
 727 mechanism. For the continuation at $f=f_{\max}$ (black lines with symbols in panel 9b),
 728 occlusion is caused by absolute linear instability (AI) when axial viscous diffusion is
 729 neglected (dot-dashed line), and by nonlinear loss of travelling-wave solutions (LP) when
 730 it is taken into account (solid line).

731 For the lowest Ca (panel 9d, case 4: $Ca=0.012$), neglecting axial viscous diffusion does
 732 not meaningfully affect Re_{\max} . It is however responsible for the formation of a second
 733 lobe on the black dot-dashed curve marked by an asterisk, which results from a change
 734 in the number of precursory ripples, as discussed w.r.t. panels 6a and 6c.

735 The nonlinear mechanism by which axial viscous diffusion precipitates occlusion is

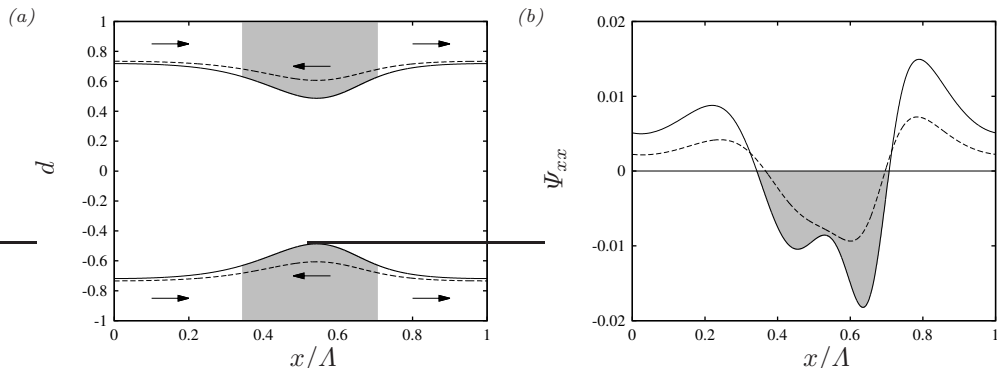


FIGURE 10. Mechanism delaying occlusion due to axial viscous diffusion. Data correspond to the two solution points marked by a cross and a diamond in panel 9a. Solid lines: diamond in panel 9a, $\text{Re}=1.47\times 10^{-4}$; dashed lines: cross in panel 9a, $\text{Re}=1.0\times 10^{-4}$. (a) Surface profiles with zones of negative (grey) and positive (white) Ψ_{xx} ; (b) normalized differential normal axial viscous stress Ψ_{xx} according to (3.2). Axial normal viscous stresses counteract gravity in the wave fronts, tending to steepen the trailing and flatten the leading wave front.

736 illustrated in figure 10. Panel 10a represents surface profiles corresponding to the two
 737 points marked by a diamond and a cross in panel 9a. The solid profile in panel 10a
 738 corresponds to the point marked by a diamond in panel 9a and the dashed profile to
 739 the point marked by a cross. In panel 10b, we have plotted corresponding profiles of the
 740 normalized axial normal viscous force Ψ_{xx} :

$$\Psi_{xx} = \frac{\text{Fr}^2}{\text{Re}} \frac{\partial_x F_{xx}}{\pi(1-d^2)}, \quad F_{xx} = 2\pi \int_d^1 \partial_x u r dr, \quad (3.2)$$

741 where F_{xx} is the (dimensionless) axial viscous force acting on the cross section of the
 742 liquid film. Its differential $dF_{xx} = \partial_x F_{xx} dx$ yields the resulting axial normal viscous force
 743 acting on a slice of liquid film. In (3.2), we have normalized dF_{xx} with the differential
 744 gravitational force to obtain Ψ_{xx} .

745 Grey and white areas underneath the solid curves in panels 10a and 10b identify regions
 746 where the axial normal viscous force is directed counter to ($\Psi_{xx} < 0$) or in the direction of
 747 ($\Psi_{xx} > 0$) gravity. Based on this, the arrows in panel 10a illustrate the resulting action of
 748 axial normal viscous stresses. This action tends to steepen the trailing front of the surface
 749 wave (where the residual film and the wave hump are pushed toward one another) and
 750 elongate the leading wave front (where residual film and wave hump are pulled away
 751 from one another). It counters the gravity-induced compression of the leading wave front
 752 and elongation of the trailing wave front and thus weakens the saturation mechanism
 753 discussed in section 3.3. The strength of the effect increases with increasing Reynolds
 754 number, as evidenced by comparing the two profiles in panel 10b and this explains why
 755 the solid and dot-dashed lines in panel 9a diverge with increasing Re .

756 Axial viscous diffusion also greatly affects the wave speed and the streamline pattern
 757 in the wave-fixed reference frame. In panel 9c, we have replotted the continuation curves
 758 from panel 9a in terms of the fluid velocity at the wave crest $u(d_{\min})$ normalized by the
 759 wave celerity c . When $u(d_{\min}) > c$, a moving-frame vortex develops in the wave hump.
 760 Such waves are known as roll waves and the grey area in panel 9c delimits their existence.
 761 The limit point on the solid black line (filled circle) lies within this region, while the limit
 762 point on the dot-dashed line (asterisk) does not. This is illustrated by the corresponding
 763 streamline patterns in figure 11. Also, we see that the roll wave in panel 11a conveys with

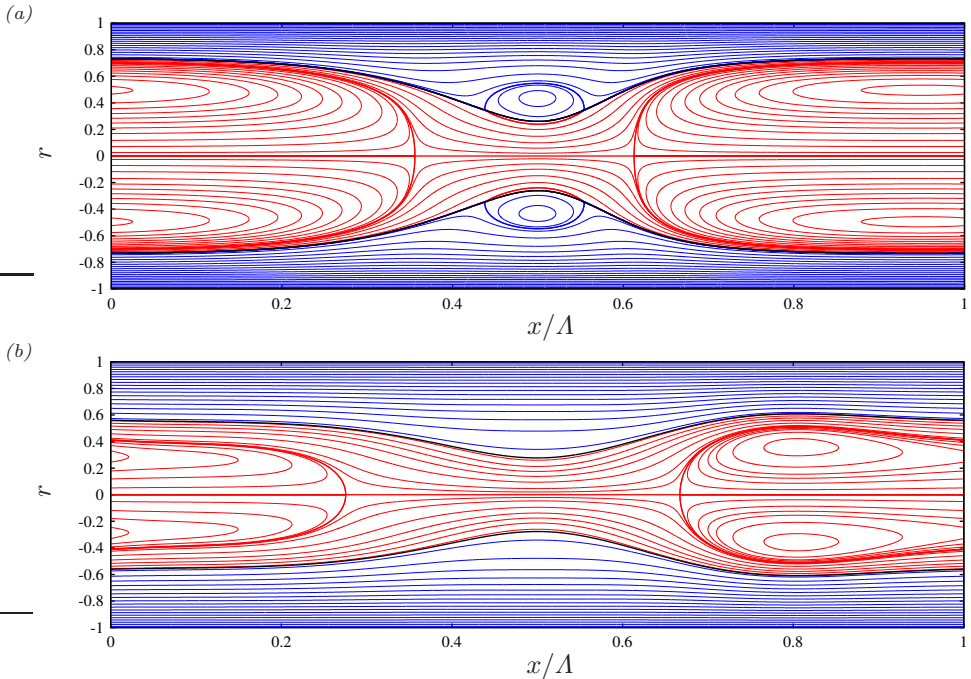


FIGURE 11. Streamlines in the wave-fixed reference frame for the marked limit points (LP) in panel 9c. Blue lines correspond to liquid film and red lines to core gas flow. (a) Full model (2.5): filled circle in panel 9c. The wave hump contains a vortex; (b) no axial viscous diffusion, i.e. $J_j=K_j=L_j=M_j=0$ in (2.5): asterisk in panel 9c. No vortex is predicted in the wave hump.

764 it a large gas bubble containing a toroidal vortex. This particular flow pattern results
 765 from the aerostatic pressure difference imposed here, i.e. $\Psi=1$. Other gas flow scenarios
 766 will be discussed in section 3.6. Finally, we point out that the lower branches in panel
 767 9 are the stable ones, and that only the full model, which accounts for axial viscous
 768 diffusion, predicts roll wave solutions on these branches.

3.5. Role of inertia

770 Inertia constitutes the growth mechanism of the Kapitza instability, which is respon-
 771 sible for the formation of surface waves on planar falling liquid films, and which becomes
 772 relevant in our current problem when Re is sufficiently large. This is the case for the low-
 773 viscosity silicone oil film (case 4). In figure 12, we have represented nonlinear travelling-
 774 wave solutions (panel 12a) and dispersion curves of the linear spatial growth rate α_i
 775 (panel 12b) for this case. Solid curves were obtained with our full model (2.5), and
 776 dashed curves by neglecting inertia, i.e. by setting $S_i=F_{ij}=G_{ij}=0$ in (2.5) and (2.11).

777 In panel 12a, we confront two types of travelling-wave continuations. On the blue
 778 lines without symbols, we have fixed the wavelength $\Lambda=12.56$. In this case, the effect of
 779 inertia is purely nonlinear. We see that this effect significantly advances the limit point
 780 of the solid blue versus the dashed blue curve (by approximately 20%). Inertia increases
 781 the cumulated strength of the destabilizing mechanisms (Plateau-Rayleigh and Kapitza
 782 instabilities) versus the stabilizing ones (capillarity and viscous dissipation). This limits
 783 the ability to saturate nonlinear travelling waves to smaller amplitudes, i.e. lower Re .

784 On the black lines with symbols, we have imposed $f=f_{\max}$. Here, the effect of inertia

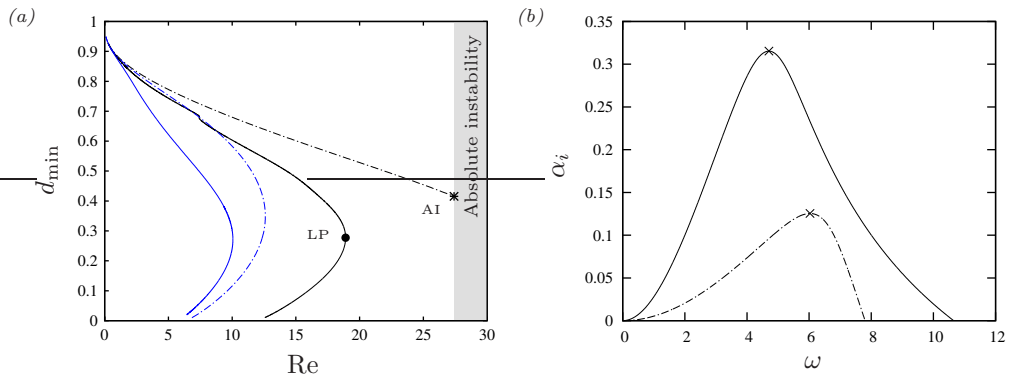


FIGURE 12. Precipitation of occlusion due to inertia. Case 4: low-viscosity silicone oil, $Bo=0.993$. Solid lines: full model (2.5); dot-dashed lines: no inertia, $S_i=F_{ij}=G_{ij}=0$ in (2.5) and (2.11). (a) Nonlinear travelling-wave solutions. Black lines with symbols: $f=f_{\max}$; blue lines without symbols: $A=12.56$; (b) dispersion curves of linear spatial growth rate α_i : $Re=15.4$.

is even stronger, as it additionally affects linear wave selection by determining the spatially most amplified wave frequency f_{\max} . The linear dispersion curves in panel 12b, where $Re=15.4$, illustrate this effect. When inertia is taken into account (solid curve), $\omega_{\max}=2\pi f_{\max}$ moves to smaller frequencies, which we have shown to precipitate the loss of travelling-wave solutions (panel 6a in §3.2). Comparing the solid and dashed lines in panel 12a, we see that inertia, similar to axial viscous diffusion, also dictates the nature of the occlusion mechanism. When it is taken into account, occlusion results from the loss of travelling-wave solutions at the limit point (LP) marking the upper occlusion bound Re_{\max} . When it is neglected, occlusion occurs to to absolute instability (AI).

In addition to shifting Re_{\max} , inertia also changes the nature of the occlusion bound in panel 12a. If inertia is neglected, Re_{\max} is dictated by absolute instability (AI, asterisk), otherwise, it is dictated by a nonlinear turning point (LP, filled circle). This qualitative change was also observed for the role of axial viscous diffusion in figure 9.

In the case of the classical Plateau-Rayleigh configuration, $Bo \rightarrow 0$, inertia only affects the dynamics of the film's evolution (Dietze & Ruyer-Quil 2015) but not the occlusion limit itself, because the latter is determined by a static equilibrium state (Everett & Haynes 1972).

3.6. Role of core gas flow

The gas in the core of the cylindrical tube can affect the liquid film falling down its inner wall in two ways: (i) through the normal and tangential interfacial viscous stresses τ_g^n and τ_g^t , which are scaled by Π_μ in (2.3), and (ii) through the interfacial gas pressure p_g , which is scaled by Π_ρ in (2.3). Up until now, we have assumed that the gas is subject to an aerostatic pressure difference, $\Psi=1$, meaning that gravity is fully compensated in the gas. In that case, the gas flow is enslaved to the hydrodynamics of the liquid film and both the above effects are negligible. Nonetheless, this one-way coupling produces intricate flow structures in the gas, as has been suggested by panel 11a and will be discussed further based on panel 14a.

Conversely, when the gas flows counter-currently at a Reynolds number Re_g of sufficient magnitude, it *does* affect the hydrodynamics of the liquid film, and this two-way coupling can significantly precipitate the upper occlusion bound Re_{\max} . We show this in figure 13 based on case 4, which produces surface waves of sufficient amplitude to significantly

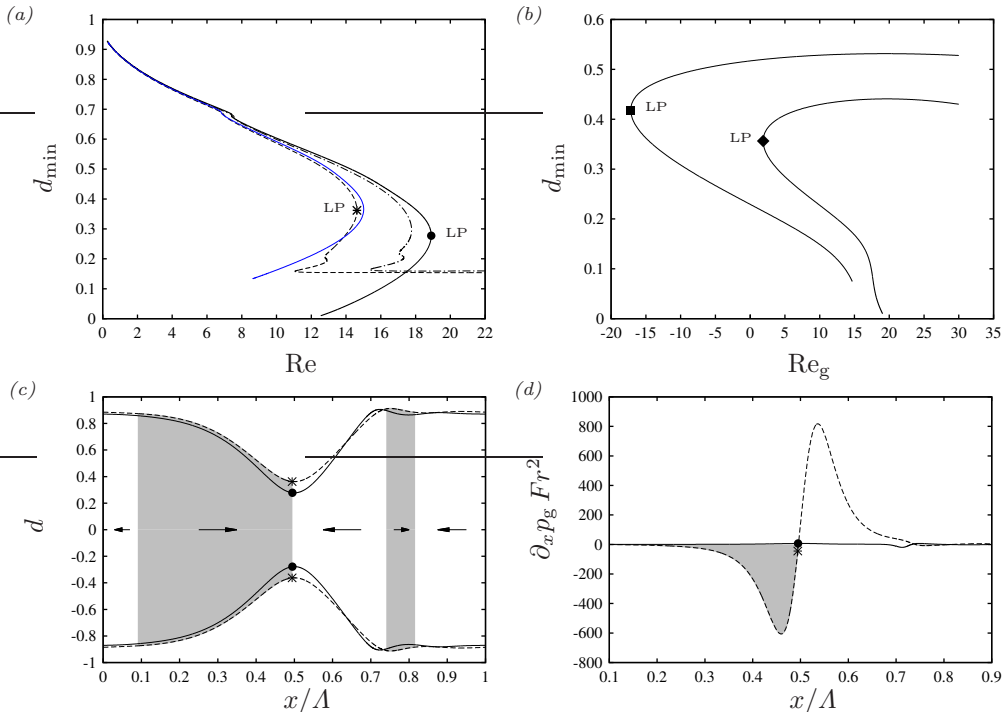


FIGURE 13. Precipitation of occlusion due to a counter-current gas flow. Case 4. (a) Travelling-wave continuation at $f=f_{\max}$. Solid: aerostatic pressure drop, $\Psi=1$; dashed: counter-current gas flow, $Re_g=-17.27$; solid blue line without symbol: $\Pi_\mu=0$ in (2.5), $Re_g=-17.27$; dot-dashed: $\Pi_\rho=0$ in (2.5), $Re_g=-17.27$; (b) continuation at $V_1=\text{const}$ and $f=f_{\max}$. Square: $V_1/\pi/R^3=2.435$; diamond: $V_1/\pi/R^3=2.770$; (c) wave profiles corresponding to the asterisk and filled circle in panel a; (d) corresponding profiles of gas pressure gradient $\partial_x p_g$ according to (2.5c) (symbols mark position of wave maximum). Grey/white zones between the dashed profiles in panels c, d demarcate regions of negative/positive $\partial_x p_g$. Arrows in panel c indicate action of gas pressure gradient on the liquid film.

816 constrict the core gas flow. Panel 13a represents travelling-wave solutions obtained by
 817 continuing Re at $f=f_{\max}$ for different gas flow configurations. The solid black curve with
 818 a filled circle at the limit point corresponds to $\Psi=1$, and the dashed curve to a counter-
 819 current gas flow with $Re_g=-17.27$. Comparing these two curves, we see that Re_{\max} is
 820 significantly precipitated due to the counter-current gas flow (by roughly 25%). We have
 821 checked that the gas flow does not meaningfully affect the most amplified frequency
 822 f_{\max} , and thus this precipitation is a nonlinear effect. **The dashed curve also displays**
 823 **two qualitative changes. First, its lower branch turns forward at a second, lower, limit**
 824 **point, producing travelling-wave solutions of constant amplitude that exist far beyond**
 825 **Re_{\max} . However, as we show in appendix C, these solutions are inaccessible in a real**
 826 **system. Thus, Re_{\max} remains a representative occlusion bound also in the counter-current**
 827 **configuration. Second, solutions on the portion of the curve between the asterisk and the**
 828 **new limit point are stable, in contrast to those on the lower branch of the solid black**
 829 **curve, where $\Psi=1$.**

830 Panel 13b illustrates the effect of the gas flow in another way. Here, Re_g is varied at a
 831 fixed liquid volume V_1 , while maintaining $f=f_{\max}$. Such a scenario may be relevant for

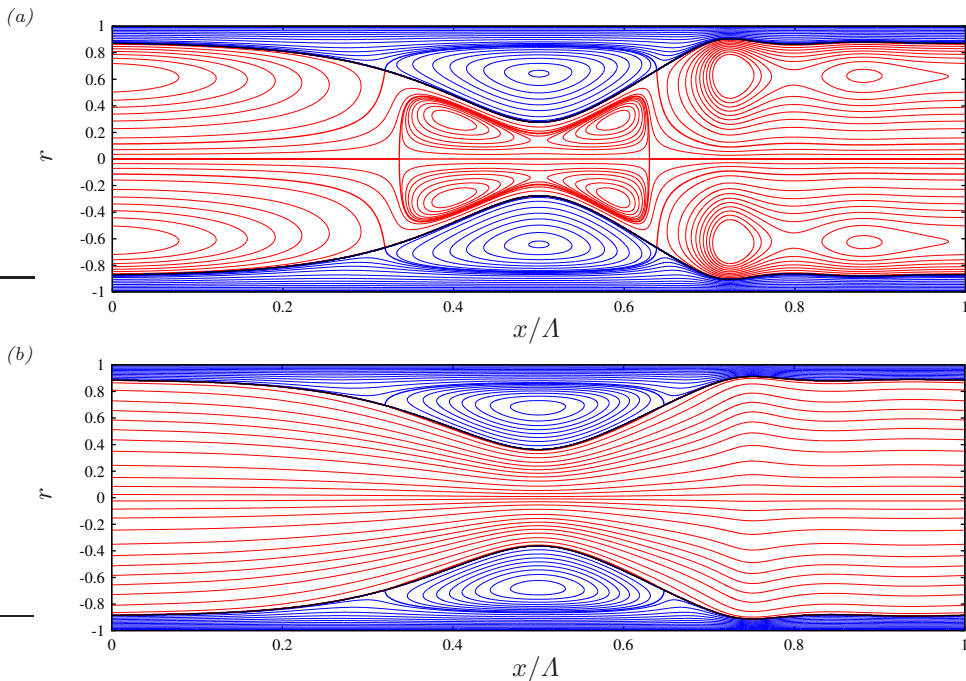


FIGURE 14. Streamlines in the wave-fixed reference frame corresponding to the marked limit points (LP) in panel 13a. Within the film, liquid below the vortex flows from right to left. (a) Aerostatic gas pressure drop (filled circle in panel 13a): $\Psi=1$, $\text{Re}=18.9$, $\Lambda=6.3$; (b) counter-current gas flow (asterisk in panel 13a): $\text{Re}_g=-17.27$, $\text{Re}=14.6$, $\Lambda=5.7$. The gas, flowing from right to left, is constricted by the wave hump, similar to a de Laval nozzle.

832 mucus films in pulmonary capillaries. We see that travelling-wave solutions are lost when
 833 the magnitude of the counter-current gas flow $|\text{Re}_g|$ is increased beyond a limit point.

834 The effect of the gas flow on the occlusion bound Re_{max} observed in panel 13a results
 835 from the pressure coupling between gas and liquid and not from the gaseous interfacial
 836 viscous stresses. This is evidenced by the curves without symbols in panel 13a, which
 837 pertain to different limits of the full-model continuation at $\text{Re}_g=-17.27$ (dashed curve).
 838 The blue solid curve without symbol pertains to the limit $\Pi_\mu=0$ and the dot-dashed curve
 839 to the limit $\Pi_\rho=0$. Deactivating the gaseous viscous stresses ($\Pi_\mu=0$, solid blue curve
 840 without symbols), changes Re_{max} very little. By contrast, deactivating the gas pressure
 841 effect ($\Pi_\rho=0$, dot-dashed curve), almost entirely negates the gas-induced precipitation
 842 of Re_{max} versus the aerostatic reference case (solid black curve with filled circle).

843 To elucidate the role of the gas pressure p_g , panels 13c and 13d represent wave profiles
 844 and corresponding profiles of the pressure gradient $\partial_x p_g$ for the two marked limit points
 845 (LP) in panel 13a. Thereby, $\partial_x p_g$ is determined from (2.5c) and corresponds to the
 846 gas pressure gradient at the film surface $\partial_x p_g|_{r=d}$. We have dropped the accompanying
 847 subscripts for convenience. In panel 13d, $\partial_x p_g$ is multiplied with Fr^2 , in order to normalize
 848 the actual pressure gradient with the aerostatic one. Grey/white zones between the
 849 dashed lines in panels 13c and 13d distinguish regions of negative/positive $\partial_x p_g$ in
 850 the gas. In addition, figure 14 represents streamlines in the wave-fixed reference frame
 851 corresponding to the wave profiles in panel 13c.

852 Focussing on the counter-current case, panel 14b, we see that the wave hump produces
 853 a constriction through which the gas (flowing from right to left) must pass, similar to a

de Laval nozzle that first accelerates and then decelerates the flow. This produces strong positive/negative pressure gradients to the right/left of the wave maximum (see dashed line in panel 13d) and these tend to push the liquid within the film toward the wave hump (arrows in panel 13c). This mechanism tends to increase the wave amplitude for a given Re and thus to advance the occlusion bound Re_{\max} . It requires a sufficiently strong relative motion between the traveling wave and the gas. This does not necessarily require an upward gas flow. Indeed, the diamond-marked curve in panel 13b shows that occlusion may be brought about even when the gas is co-current, at least if $|Re_g|$ is sufficiently small.

In the aerostatic case, $\Psi=1$, axial pressure variations in the core are very weak (solid line in panel 13d) and the gas has no incidence on the occlusion limit. Vice versa, the flow structure in the gas is strongly affected by the liquid film. We see this in panel 14a, which pertains to case 4 (low-viscosity silicone oil), and also in panel 11a, which pertains to case 1 (high-viscosity silicone oil). In both examples, the gas flow is enslaved to the liquid surface flow (through equation 2.3a), which exhibits interfacial stagnation points around the wave hump, as a result of the moving-frame vortex in the liquid film. Due to this, the gas flow is divided into an intricate system of vortices. The constellation of these vortices is dictated by the strength of the liquid vortex in the wave hump.

3.7. Occlusion scenarios in a spatially evolving film

In section 3.2, we introduced the conservative occlusion bounds Re_0 and Re_{\max} based on the limit of travelling-wave solutions and delimited three regimes for a naturally evolving wavy falling liquid film: (i) impossible occlusion, when $Re < Re_0$, (ii) conditional occlusion, when $Re_0 < Re < Re_{\max}$, and (iii) certain occlusion, when $Re > Re_{\max}$. We now demonstrate these regimes based on spatio-temporal computations with our model (2.5), where we have mimicked naturally-evolving waves through the noisy inlet condition (2.6b), using $\epsilon_2=10^{-5}$. For the gas, we have imposed $\Psi=1$.

We start by reproducing two of the occlusion experiments of Dao & Balakotaiah (2000), i.e. their experimental runs 20 and 13 which identified the experimental occlusion point at $Re=0.0497$ and $Re=0.258$, respectively. These two runs correspond to our cases 2 and 3 in table 1, for which we have determined the lower/upper occlusion bounds in §3.2 as $Re_0=0.012/Re_{\max}=0.038$ (panel 5c), and $Re_0=0.075/Re_{\max}=0.39$ (panel 5d), respectively. Based on this, experimental run 20 (our case 2) lies in the region of certain occlusion and experimental run 13 (our case 3) in the region of conditional occlusion. This is confirmed by panels 15a and 15b, which represent travelling-wave solutions continued in terms of the wave frequency f (right abscissae) and dispersion curves of the linear growth rate α_i (left abscissae) for these two runs.

The experiments of Dao & Balakotaiah (2000) were performed in a long vertical tube equipped with a conductance probe that allowed to detect occlusion locally. However, no information on the film's surface dynamics upstream of this point was available. We provide this missing information in panels 15c and 15d, which represent snapshots of our spatio-temporal computations reproducing experimental runs 20 and 13. These computations were performed on an $L^*=1$ m domain. We see that the two cases reach occlusion by two very different routes, as a result of distinct wave dynamics.

For experimental run 20 (our case 2), most of the dispersion curve in panel 15a (grey area) lies beyond the limit point of travelling wave solutions ($f_{\max} < f_{LP}$). Thus, the most amplified surface waves emerging from the linear regime don't possess any saturated travelling state and inevitably cause occlusion by extending their growth into the nonlinear regime (panel 15c). This is occlusion scenario I, which we had already observed for case 1 (high-viscosity silicone oil) in figure 4. Supplementary movie M2 shows

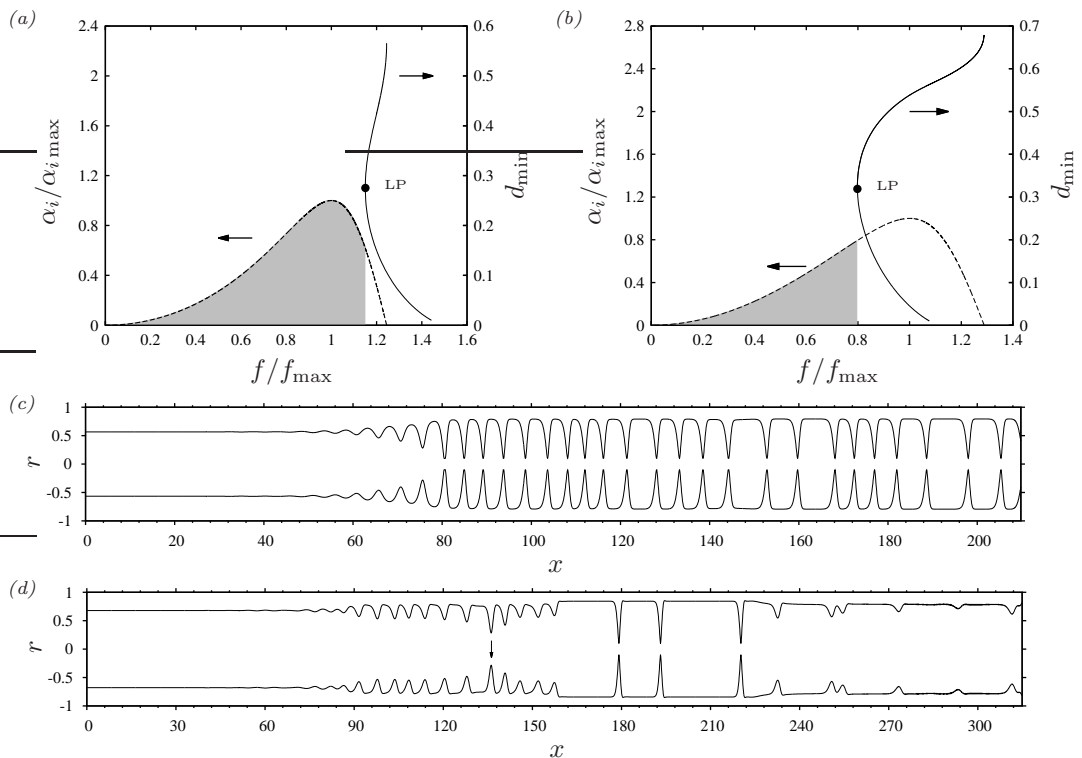


FIGURE 15. Different routes to occlusion in a spatially evolving film. Computations of experimental runs 20 (panels *a,c*) and 13 (panels *b,d*) in Dao & Balakotaiah (2000). (*a,b*) Travelling wave solutions (right abscissae) at $\text{Re}=\text{const}$, and dispersion curves of the linear spatial growth rate α_i (left abscissae). Grey zones distinguish linear waves that have no saturated travelling state; (*c,d*) spatio-temporal computations on an $L^*=1$ m domain with inlet noise (2.6*b*); (*a,c*) experimental run 20: case 2 in table 1, $\text{Re}=0.0497$ (regime of certain occlusion, scenario I); (*b,d*) experimental run 13: case 3 in table 1, $\text{Re}=0.258$ (regime of conditional occlusion, scenario II). Arrow in panel *d* marks a coalescence event triggering occlusion.

903 the computation from panel 15c in action. We remind the reader that the unphysical
 904 plug reopening observed therein (and in supplementary movie M3) is due to the crude
 905 numerical core radius limitation introduced in section 2.1. First results in appendix E
 906 suggest that this artefact is negated by our improved WRIBL model (figure 22).

907 By contrast, for experimental run 13 (our case 3), the most amplified linear waves lie
 908 well within the range of travelling-wave solutions ($f_{\max} > f_{\text{LP}}$ in panel 15b). Occlusion
 909 must thus occur through a different route, as evidenced by the wave profile in panel
 910 15d. In the first part of the tube ($x \leq 130$), a quite regular train of saturated-amplitude
 911 travelling waves develops. These result from linear wave selection and their minimal core
 912 radius d_{\min} is far from reaching the tube axis. However, individual waves within the wave
 913 train are quite narrowly spaced and thus prone to the secondary subharmonic/sideband
 914 instabilities typically associated with single-humped waves in planar falling liquid films
 915 (Liu & Gollub 1993; Chang *et al.* 1993). These instabilities result from wave interactions
 916 triggered by residual noise and lead to wave coalescence, which is the first step in the
 917 so-called wave coarsening dynamics identified by Chang *et al.* (1996*b*). This cascaded dy-
 918 namics produces ever longer, more dangerous, waves by successive coalescence/absorption
 919 events and thus represents an inherent route toward occlusion. The arrow in panel 15d

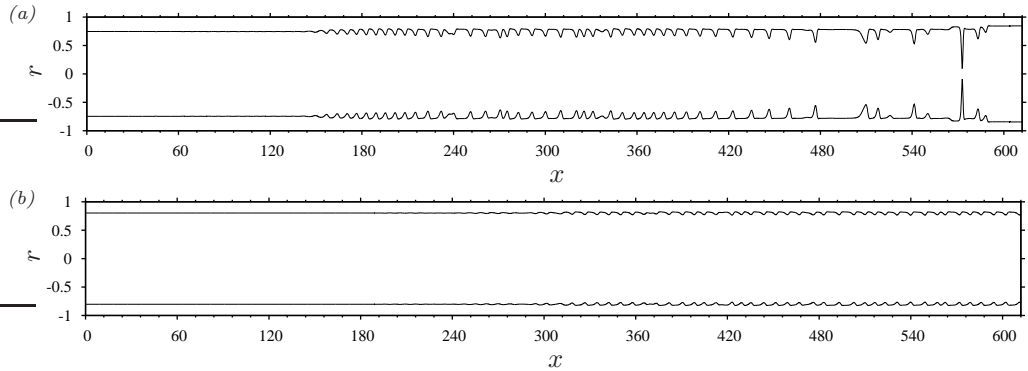


FIGURE 16. Computations of case 3 ($Re_0=0.075$, $Re_{max}=0.39$; panel 5b) at lower Re , showing a downstream displacement of the occlusion point w.r.t. panel 15d. Spatio-temporal computations on an $L^*=2$ m domain with inlet noise (2.6b). (a) $Re=0.14$: regime of conditional occlusion. Occlusion (through scenario II) occurs much further downstream than in panel 15d; (b) $Re=0.07 < Re_0$: regime of impossible occlusion. Surface waves are extremely small.

920 highlights one such coalescence event, which produces a wave of greater amplitude that
 921 will occlude the tube and subsequently absorb several smaller waves downstream.

922 This is occlusion scenario II, which is intermittent because the initiating wave coa-
 923 lesence is occasional, in contrast to scenario I (panel 15c), where (almost) every wave
 924 grows to occlude the tube. Due to this intermittence, gas bubbles resulting from successive
 925 occlusion events are much more unevenly distributed. Supplementary movie M3 shows
 926 the computation from panel 15d in action.

927 We now focus on case 3 and compute the spatio-temporal wave evolution for values of
 928 Re below the experimental occlusion threshold $Re=0.258$ determined in run 13 of Dao &
 929 Balakotaiah (2000). This experimental threshold lies well within the region of conditional
 930 occlusion, which is bounded by $Re_0=0.075$ and $Re_{max}=0.393$ (panel 5d).

931 Panel 16a represents a spatio-temporal computation at a lower Reynolds number
 932 $Re=0.14 > Re_0$, which still lies in the conditional occlusion regime. This computation
 933 was performed on a domain of $L^*=2$ m in length, i.e. twice longer than the one in
 934 panel 15d. We see that occlusion still occurs, through scenario II, but that the occlusion
 935 point has shifted greatly downstream w.r.t. panel 15d. The reason for this is that the
 936 frequency/wavelength of the limiting travelling waves greatly decreases/increases with
 937 decreasing Re (see panel 5d) and, thus, much more space is needed for these to develop
 938 from the coarsening dynamics. The downstream shift in the occlusion point explains
 939 why Dao & Balakotaiah (2000), who checked for occlusion in a fixed region, found an
 940 experimental threshold for Re that is greater than the lower conservative bound Re_0 . It
 941 also clearly shows that occlusion in the conditional regime (through scenario II) depends
 942 on whether the tube is sufficiently long to accommodate formation of those waves that
 943 are able to cause occlusion. As these waves may be much longer than those emerging
 944 from linear selection, occlusion may require unrealistically long tube lengths, depending
 945 on Re . Supplementary movie M4 shows the computation from panel 16a in action.

946 Conversely, occlusion in an infinitely long tube will eventually always occur if Re
 947 lies within the conditional regime, at least for a naturally evolving film. This is due to
 948 the nature of the coarsening dynamics, which halts only after truly solitary waves have
 949 formed. Thus, to avoid occlusion in an infinitely long tube, Re must be decreased below
 950 the lower conservative bound Re_0 , where even solitary waves are too small to cause

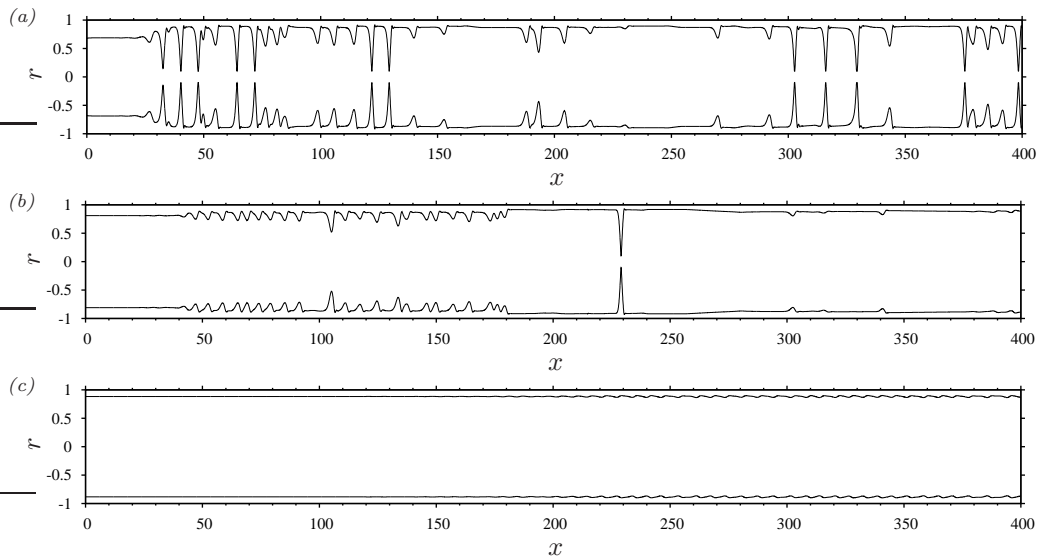


FIGURE 17. Different occlusion scenarios for case 4 ($Re_0=1.5$, $Re_{\max}=18.9$; panel 6b). Spatio-temporal computations on an $L^*=1$ m domain with inlet noise (2.6b). (a) $Re=19 > Re_{\max}$: regime of certain occlusion (scenario I); (b) $Re=5$: regime of conditional occlusion (scenario II); (c) $Re=1.25 < Re_0$: regime of impossible occlusion. Surface waves are extremely small

951 occlusion. Panel 16b shows a computation under such conditions, i.e. $Re=0.07 < Re_0$.
 952 Although occlusion is indeed avoided, surface waves are extremely small in amplitude,
 953 which thwarts their beneficial effect on heat and mass transfer (Yoshimura *et al.* 1996;
 954 Albert *et al.* 2013). This underlines the conservative nature of the lower occlusion bound
 955 Re_0 . We will show in the next section that there is another way to prevent occlusion,
 956 namely through coherent inlet forcing in the conditional occlusion regime, which allows
 957 maintaining surface waves of significant amplitude.

958 Finally, figure 17 shows snapshots of three representative spatio-temporal computa-
 959 tions for case 4 (low-viscosity silicone oil), where inertia, which drives the the Kapitza
 960 instability, is relevant. Panels 17a, 17b, and 17c correspond to the regimes of certain,
 961 conditional, and impossible occlusion. These display the same main features observed for
 962 the high-viscosity liquids (panels 15c, 16a, and 16b), only that the length scales of the
 963 occlusion processes are much shorter.

964 3.8. Coherent inlet forcing to prevent occlusion

965 For $Re > Re_0$, travelling-wave solutions are bounded by a limiting frequency f_{LP} , below
 966 which they cannot exist and occlusion is inevitable (see panels 5d and 6b). Conversely,
 967 by increasing f above f_{LP} , travelling-wave solutions are recovered and occlusion can be
 968 avoided. We thus test the idea of forcing high-frequency waves through coherent inlet
 969 forcing in a spatially-evolving falling liquid film, in order to prevent occlusion without
 970 having to reduce Re below the conservative bound Re_0 , where surface waves all but
 971 disappear (see panels 16b and 17c).

972 This idea works only in the conditional occlusion regime, $Re_0 < Re < Re_{\max}$. Indeed,
 973 in the regime of certain occlusion, $Re > Re_{\max}$, where $f_{LP} > f_{\max}$, one would have to
 974 force waves of frequency $f > f_{\max}$. Such short waves are very sensitive to the secondary
 975 instabilities causing wave coalescence in closely-packed wave trains (Liu & Gollub 1993),

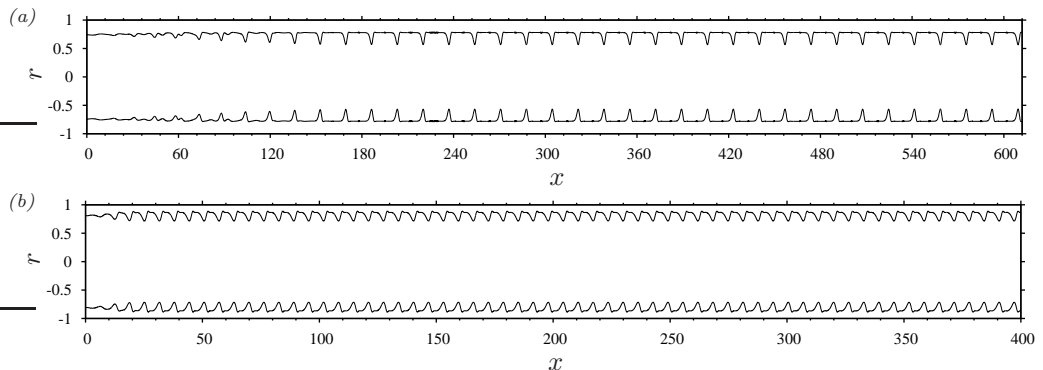


FIGURE 18. Preventing occlusion in the conditional occlusion regime, $Re_0 < Re < Re_{max}$, through coherent inlet forcing. Spatio-temporal simulations from panels 16a and 17b with additional coherent inlet forcing of frequency f and amplitude $\epsilon_1=0.1$ (2.6b). All other parameters, including the noise level ϵ_2 , remain unchanged. (a) Case 3 ($Re_0=0.075$, $Re_{max}=0.393$; panel 5d): $Re=0.14$, $f=0.5 f_{max}=0.525$; (b) Case 4 ($Re_0=1.5$, $Re_{max}=18.9$; panel 6b): $Re=5$, $f=0.5 f_{max}=1.27$. Coherent inlet forcing produces a regular train of saturated-amplitude travelling waves, allowing to prevent occlusion versus the natural evolution in panels 16a and 17b.

976 and rapidly lose the signature of the inlet forcing. By contrast, in the conditional
 977 occlusion regime, f_{LP} can be low enough (the lower Re , the lower f_{LP}) to allow forcing
 978 a wave train that is not subject to secondary instability.

979 We demonstrate this by running the spatio-temporal computations in panels 16a (case
 980 3) and 17b (case 4) again with additional coherent inlet forcing. For this, we activate the
 981 monochromatic perturbation in (2.6b) with a relative amplitude $\epsilon_1=0.1$. Meanwhile, the
 982 inlet noise remains active and its level unchanged $\epsilon_2=10^{-5}$. We stress that ϵ_2 in (2.6b) is
 983 the scale factor of a Fourier series which 1000 terms. Thus, the actual noise amplitude
 984 is much greater than suggested by the value of ϵ_2 . It is about 10% of ϵ_1 for the runs
 985 presented here. The forcing frequency f is chosen greater than the limit value f_{LP} of
 986 travelling-wave solutions, as obtained from panels 5d (case 3, $Re=0.14$, $f_{LP}=0.41 f_{max}$)
 987 and 6b (case 4, $Re=5$, $f_{LP}=0.35 f_{max}$), respectively.

988 Panels 18a and 18b show the results of our spatio-temporal computations with ad-
 989 ditional coherent inlet forcing and are to be compared directly to panels 16a and 17b,
 990 where the wave dynamics is purely noise-driven. We see that the additional coherent
 991 inlet forcing produces a regular train of saturated-amplitude travelling waves that do not
 992 occlude the tube. This wave train is maintained over the entire length of the domain
 993 and thus robust w.r.t. to secondary instability. In contrast to panels 16b and 17c, where
 994 occlusion was avoided by reducing Re below the lower conservative bound Re_0 , the falling
 995 films in panels 18a and 18b display quite substantial surface waves, expected to be much
 996 more beneficial for inter-phase heat and mass transfer.

997 4. Conclusion

998 We have studied numerically the occlusion of a narrow vertical cylindrical tube by
 999 an axisymmetric wavy falling liquid film in contact with a laminar core gas flow. We
 1000 have focused on conditions where the effect of gravity is at least comparable to that of
 1001 capillarity, i.e. $Bo \geq 1$, and the gas Reynolds number Re_g is quite low. In that limit,
 1002 occlusion is caused by spatially growing waves and not by absolute linear instability.

1003 These waves are generated by a combination of the Plateau-Rayleigh instability, gravity-
 1004 driven advection, and the Kapitza instability.

1005 Using the low-dimensional model introduced in Dietze & Ruyer-Quil (2015), which
 1006 had been applied only to gravity-free films, we have performed spatio-temporal compu-
 1007 tations of spatially-evolving falling films and computed travelling-wave solutions through
 1008 numerical continuation. Our model extends upon the earlier works of Trifonov (1992),
 1009 Camassa *et al.* (2014, 2017), Zhou *et al.* (2016), Liu & Ding (2017), and Ding *et al.*
 1010 (2019) by accounting for axial viscous diffusion and inertia. These effects are needed to
 1011 accurately predict occlusion for the real liquids studied here (cases 1-4 in table 1). We
 1012 have validated our model computations with DNS (appendix A and panel 5d).

1013 Travelling-wave solutions are lost when the liquid Reynolds number Re is increased
 1014 beyond a limit point (LP), low-frequency/long waves being more dangerous (smaller
 1015 Re_{LP}) than high-frequency/short waves (greater Re_{LP}). By numerically reproducing the
 1016 occlusion experiments of Camassa *et al.* (2014), we have proved that surface waves causing
 1017 occlusion systematically lie beyond this limit of travelling-wave solutions, thus validating
 1018 the conjecture formulated by these authors.

1019 Depending on how occluding waves emerge in a spatially evolving film, either directly
 1020 from linear wave selection (scenario I), or subsequent secondary instability and wave
 1021 coarsening (scenario II), we have distinguished two possible occlusion scenarios. By
 1022 reproducing several occlusion experiments with our own spatio-temporal computations,
 1023 we have shown that occlusion scenario I (panels 4a and 15c, movie M2) applies to the
 1024 experiments of Camassa *et al.* (2014) and run 20 in Dao & Balakotaiah (2000), while
 1025 scenario II (panel 15d, movie M3) applies to run 13 in Dao & Balakotaiah (2000).

1026 We have delimited scenarios I and II based on an upper conservative occlusion bound
 1027 Re_{max} , which corresponds to the limit point of travelling-wave solutions at the spatially
 1028 most amplified frequency f_{max} of linear waves. And, a lower conservative bound Re_0 ,
 1029 below which travelling-wave solutions always exist, no matter how great the wavelength
 1030 (Ding *et al.* 2019). Determining Re_{max} requires computing f_{max} and thus we have
 1031 simultaneously solved the linear stability problem in our numerical continuations. This
 1032 had not been attempted in previous studies (Camassa *et al.* 2014; Ding *et al.* 2019).

1033 Based on the upper and lower conservative bounds Re_{max} and Re_0 , as well as spatio-
 1034 temporal computations, we have delimited three possible regimes for a naturally evolving
 1035 wavy film: (i) certain occlusion: $Re > Re_{max}$. The most amplified surface waves, which
 1036 typically emerge in an experiment, do not possess travelling states. Occlusion is inevitable
 1037 and occurs through scenario I; (ii) conditional occlusion: $Re_0 < Re < Re_{max}$. Occlusion
 1038 is theoretically possible through scenario II (for long enough waves), but does not
 1039 necessarily occur in a real system. That depends on whether the coarsening dynamics
 1040 can produce sufficiently long waves and whether the tube is long enough to accommodate
 1041 this (panels 15d and 16a, movies M3 and M4); (iii) impossible occlusion: $Re < Re_0$. All
 1042 possible surface waves, no matter how long, are safe.

1043 We have shown that occlusion can be actively prevented in the regime of conditional
 1044 occlusion ($Re_0 < Re < Re_{max}$) by forcing waves of sufficiently high frequency through
 1045 coherent inlet forcing (panels 18a and 18b). This allows to maintain surface waves of non-
 1046 negligible amplitude, in contrast to the regime of impossible occlusion ($Re < Re_0$) where
 1047 waves are almost invisible (panels 16b and 17c). Given the well documented positive effect
 1048 of surface waves on inter-phase heat/mass transfer (Yoshimura *et al.* 1996), coherent inlet
 1049 forcing is an attractive route to enhance transfer while avoiding occlusion.

1050 We have computed the lower and upper conservative bounds Re_0 and Re_{max} for the
 1051 four working liquids considered here (figures 5 and 6). Further, we have quantified how
 1052 key parameters (Bo and Re_g) as well as several physical effects (axial viscous diffusion

and inertia) affect the upper conservative bound Re_{\max} , which delimits the regimes of certain and conditional occlusion. We have found that gravity greatly delays this bound, significantly increasing Re_{\max} as the Bond number Bo is increased (see panel 8a). Unless Bo is very large, the height of travelling waves at $Re=Re_{\max}$ is far from reaching the tube radius. In contrast to what Dao & Balakotaiah (2000) conjectured, such solutions are thus lost abruptly and not due to the wave height reaching the tube radius continuously.

We have found that a laminar counter-current gas flow can significantly precipitate occlusion for low-viscosity liquids (low-viscosity silicone oil, case 4), where the effect of the gas pressure becomes relevant in the liquid force balance. At the strongest gas flow studied ($Re_g=-17$), we have observed a 25% reduction of Re_{\max} (panel 13a) versus a situation where the gas is quiescent. We have found that the gas affects the liquid film mainly through inter-phase pressure coupling. Surface waves locally constrict the gas flow, which is accelerated and then decelerated as it passes through (panel 14b). This produces a pressure minimum above the wave crest that sucks liquid toward the wave, tending to increase its amplitude and, thus, the danger of occlusion.

For high-viscosity liquids (high-viscosity silicone oil and aqueous glycerol solution, cases 1 and 3), axial viscous diffusion greatly precipitates occlusion, i.e. greatly reduces Re_{\max} (by 74% in panel 9a). This may be relevant for mucus films within the first five generations of the human respiratory network, where the capillary radius is large enough for gravity to be relevant (King & Macklem 1977; Lewis *et al.* 2005; Grotberg 2011).

For low-viscosity liquids (low-viscosity silicone oil, case 4), we have observed that Re_{\max} becomes large enough for inertia to be relevant ($Re_{\max}=18.9$ in panel 6a). This activates the Kapitza instability, which tends to increase the amplitude of travelling-waves, increasing the danger of occlusion. We have found that inertia significantly precipitates occlusion, decreasing Re_{\max} versus an inertialess computation (by 20% in panel 12a). This may be relevant for falling film micro-reactors (Seebauer *et al.* 2012).

Finally, we have found that neglecting axial viscous diffusion (high-viscosity liquids, panel 9a) or inertia (low-viscosity liquids, panel 12a) can change the nature of the occlusion mechanism, from being dictated by the loss of travelling-wave solutions to being dictated by absolute linear instability.

Our transient computations on long open domains have been performed with a crude numerical core radius limitation allowing to continue these past occlusion events. Although this technique does not affect the wave dynamics leading up to occlusion, which is the focus of our current study, it does not represent the physics of liquid plugs to satisfaction. To remedy this, we have introduced an improved version of our WRIBL model (2.5) by augmenting it with an additional force term (4.1), allowing to form stable travelling pseudo-plugs (figure 22). First results reported in appendix E suggest that this improved model negates the main artefact of the numerical core radius limitation, i.e. the reopening of liquid plugs. Confronting our improved model with full-fledged plug models (Ubal *et al.* 2008; Suresh & Grotberg 2005) is an enticing prospect for future work.

Appendix A: Validation of WRIBL model based on transient DNS

Figure 19 represents comparisons between our WRIBL model (2.5) and DNS using the solver Gerris (Popinet 2009). All computations were performed for case 4 (low-viscosity silicone oil), which is the most challenging. The solid and dashed curves in panel 19a represent travelling-wave solutions obtained with our model by continuing the liquid volume V_l at fixed wavelength $\Lambda=5.4$ for two different gas flow situations. The dashed line corresponds to an aerostatic gas pressure drop $\Psi=1$, and the solid line to a counter-current gas flow at $Re_g=-17.3$. We compare these data with two punctual DNS at $V_l/\pi/R^3=2.35$,

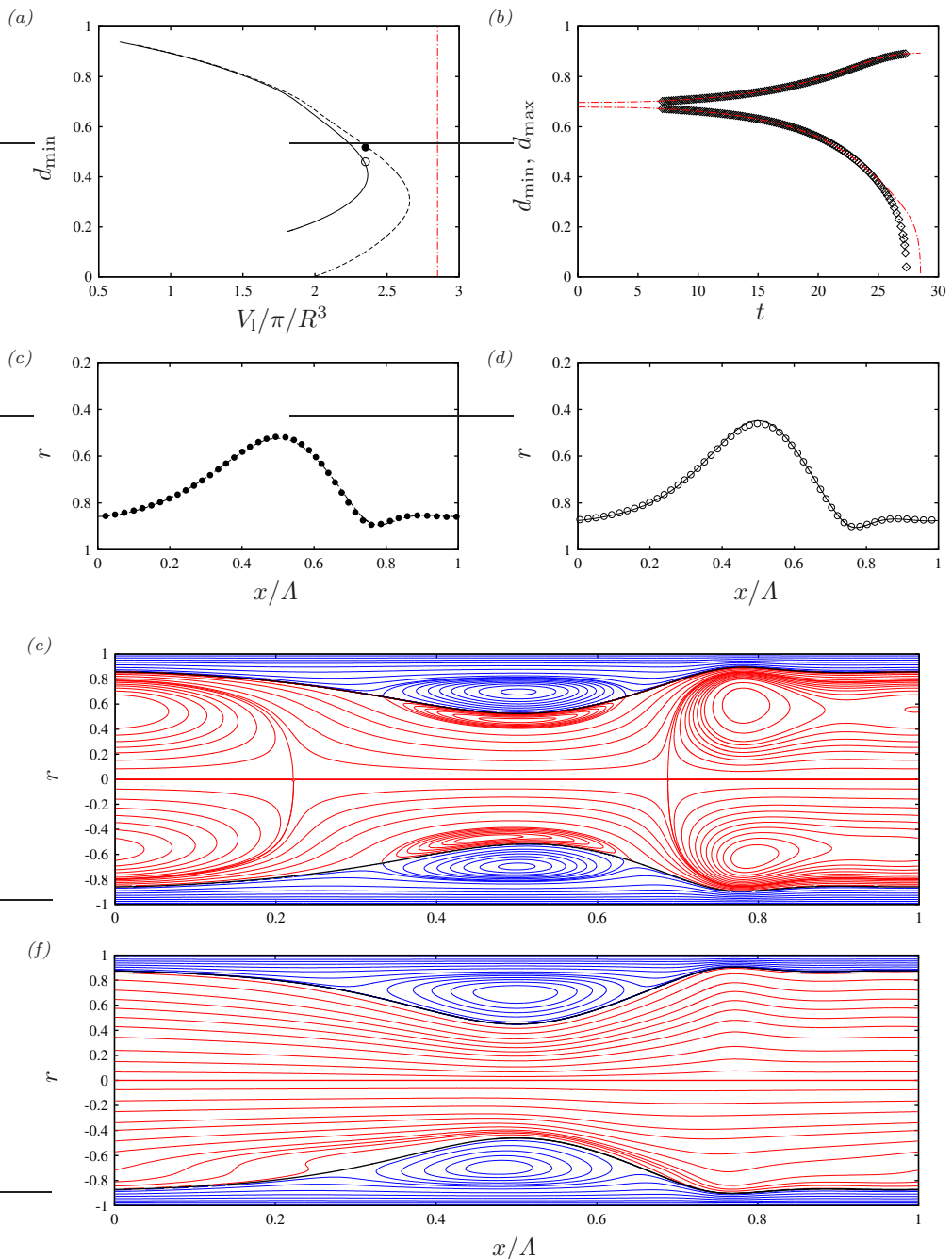


FIGURE 19. Validation of our WRIBL model (2.5) with DNS using the solver Gerris (Popinet 2009). Case 4 in table 1: low-viscosity silicone oil, $R^* = 1.5$ mm. (a) Travelling-wave solutions at fixed $\Lambda = 5.4$. Dashed line (WRIBL) and filled circle (DNS, $V_1/\pi/R^3 = 2.35$): aerostatic pressure drop, $\Psi = 1$; solid line (WRIBL) and open circle (DNS, $V_1/\pi/R^3 = 2.35$): $\text{Re}_g = -17.3$; (b) transient periodic computations with DNS solver (diamonds) and WRIBL model (dot-dashed line): $\Lambda = 5.4$, $\Psi = 1$, $V_1/\pi/R^3 = 2.85$ (vertical line in panel a); (c-d) profiles of travelling waves from panel a for $V_1/\pi/R^3 = 2.35$. Filled/open circles: DNS; dashed/solid lines: WRIBL; (e-f) streamlines in the wave-fixed reference frame for solutions in panels c and d. Top half: WRIBL; bottom half: DNS.

1101 which are marked by a filled ($\Psi=1$) and open circle ($\text{Re}_g=-17.3$), respectively. Panels 19c
 1102 and 19d represent the corresponding surface profiles at this point, as obtained from DNS
 1103 (symbols) and our model (lines). Panels 19e and 19f represent corresponding streamline
 1104 patterns in the wave-fixed reference frame. The top half of these graphs represents our
 1105 model computations and the bottom half our DNS.

1106 Finally, panel 19b compares time traces of the minimal and maximal core radius d_{\min}
 1107 and d_{\max} obtained from transient periodic computations with our model (dot-dashed
 1108 line) and the DNS solver (diamonds) for $\Lambda=5.4$, $\Psi=1$, and $V_1/\pi/R^3=2.85$ (vertical line
 1109 in panel 19a), which lies beyond the limit point of travelling-wave solutions in panel
 1110 19a. Agreement between the two data sets in panel 19b is good and both computations
 1111 produce an occlusion of the tube by the liquid film, as evidenced by the divergence of
 1112 the minimal core radius d_{\min} . This confirms that occlusion occurs beyond the limit of
 1113 travelling-wave solutions and that our model is able to capture the associated dynamics.

1114 Appendix B: Numerical procedure for travelling-wave DNS

1115 The DNS results in panel 5d were obtained by solving the full governing equations
 1116 (2.1)-(2.3) in the limit $\Pi_\mu=\Pi_\rho=0$ with a pseudo-spectral approach. For this, the liquid
 1117 velocity and pressure fields are projected on modified Chebyshev polynomials:

$$1118 \quad u_1(x, r, t) = \sum_{i=1}^n a_i(x, t) \phi_i(X), \quad p_1(x, r, t) = \sum_{i=0}^{n-1} b_i(x, t) \psi_i(X), \quad (4.1)$$

1118 where $X=2(R-r)/(R-d)-1$. The radial velocity v_1 is obtained by integrating (2.1b), i.e.
 1119 $v_1=-\frac{1}{r} \int_R^r \partial_x u_1 r dr$. The functions $\phi_i(X)$ and $\psi_i(X)$ are linear combinations of Chebyshev
 1120 polynomials of the first kind T_i :

$$1121 \quad \phi_1 = 1 + X, \quad \psi_0 = 1, \quad \psi_1 = X - 1, \quad (4.2)$$

$$1122 \quad \phi_{2i} = \psi_{2i} = T_{2i}(X) - 1, \quad \phi_{2i+1} = \psi_{2i+1} = T_{2i+1}(X) - X \quad \forall i \geq 1,$$

1121 so that $\phi_i(X = -1) = 0$, and thus the boundary conditions (2.2) are fulfilled.

1122 Writing the Navier-Stokes equations (2.1a) on the Gauss-Lobato points $X_i = -\cos(\pi i/n)$
 1123 for $i \geq 1$, and introducing the wave-fixed coordinate $\xi = x - ct$, yields $2(n-1)$ relations:

$$1124 \quad \sum_{j=0}^{n-1} \psi_j(X_i) D_\xi b_j = \mathcal{F}_i(b_i, a_i, D_\xi a_i, D_{\xi\xi} a_i, h, D_\xi h, D_{\xi\xi} h), \quad (4.3)$$

$$\frac{1}{4\text{Re}} \frac{h}{r} \sum_{j=1}^n [C_j(X_i) + I_j(X_i)] D_{\xi\xi\xi} a_i = \mathcal{G}_i(b_i, a_i, D_\xi a_i, D_{\xi\xi} a_i, h, D_\xi h, D_{\xi\xi} h),$$

1124 where $D_\xi = d/d\xi$, $C_j = \int_{-1}^X X(\phi_j)' dX$, and $I_j = \int_{-1}^X \phi_j dX$. Further, we have:

$$1125 \quad \tau_1^\dagger = \eta D_{\xi\xi\xi} a_1, \quad (4.4)$$

$$1126 \quad \tau_1^n + \text{Re } p_1 - \text{Re } \text{We}^{-1} \kappa = \eta D_\xi b_0,$$

$$1127 \quad q_1 + c \pi d^2 = \eta D_{\xi\xi\xi} h,$$

1125 and thus the free-surface dynamic conditions (2.3b)-(2.3c) and the integral continuity
 1126 equation (2.5a) are recovered in the limit $\eta \rightarrow 0$. We finally obtain the linear equation
 1127 system:

$$1128 \quad \mathbf{A} \frac{d\mathbf{U}}{d\xi} = \mathbf{B}(\mathbf{U}; \eta), \quad (4.5)$$

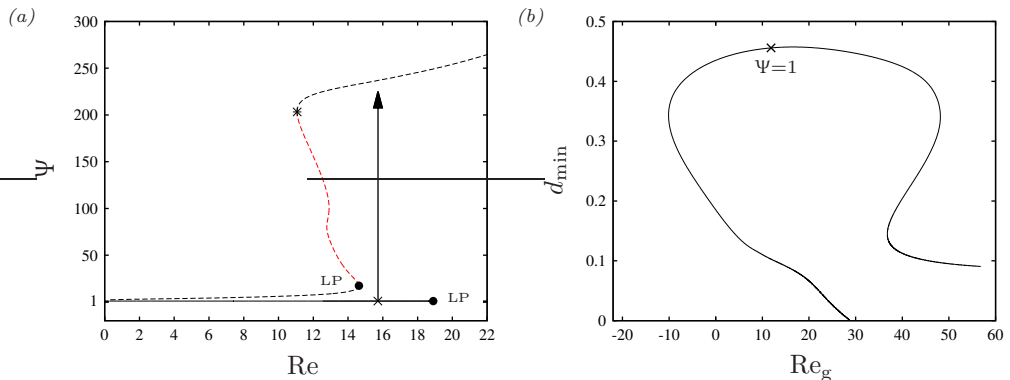


FIGURE 20. Travelling waves under the effect of a counter-current gas flow: case 4, $f=f_{\max}$. (a) New representation of the curves from panel 13a in terms of the normalized pressure gradient $\Psi=\Delta p_g Fr^2$. Solid: aerostatic pressure drop, $\Psi=1$; dashed: counter-current gas flow, $Re_g=-17.27$. Solutions between circle and asterisk (red segment) are stable. Filled circles correspond to limit points (LP) in panel 13a; (b) variation of the gas Reynolds number Re_g at $Re=15.72$. The intended continuation path is indicated by an arrow in panel a.

1128 for the unknowns $\mathbf{U}=(h, D_\xi h, D_{\xi\xi} h, a_i, D_\xi a_i, D_{\xi\xi} a_i, b_{i-1}) \forall 1 \leq i \leq n$. Inverting (4.5)
 1129 leads to an autonomous dynamical system of dimension $4n + 3$. This dynamical system
 1130 was solved with the continuation software AUTO07P (Doedel 2008), using a predictor-
 1131 corrector method (Kalliadasis *et al.* 2012). Our computations were performed with
 1132 $\eta=10^{-6}$ and $n = 20$, which we have determined based on convergence tests.

1133 Appendix C: Travelling waves on the lower branch in panel 13a

1134 We discuss further the travelling-wave solutions on the lowest branch of the dashed
 1135 curve in panel 13a, which extends beyond the limit point $Re=Re_{\max}$, as the result of
 1136 interfacial viscous stresses exerted by the gas. Panel 20a replots that curve (dashed line)
 1137 and the corresponding curve for the aerostatic configuration (solid line) in terms of the
 1138 pressure gradient $\Psi=\Delta p_g Fr^2$. The filled circles therein correspond to the limit points (LP)
 1139 in panel 13a. The segment of the dashed curve that we are interested in lies above the
 1140 asterisk, and we have checked the stability of solutions thereon, using transient periodic
 1141 computations with imposed Ψ (we recall that the red portion of the curve, between
 1142 circle and asterisk, is stable). As Re is increased on this curve segment, solutions go
 1143 from being stable to being subject to an oscillatory instability, similar to that found in
 1144 planar channels (Lavalle *et al.* to be published). In both situations, our transient periodic
 1145 computations do not produce occlusion.

1146 However, these states are inaccessible in a real system, where Re is fixed and the
 1147 counter-current gas flow is imposed through Ψ . The arrow in panel 20a indicates how Ψ
 1148 would need to be varied to attain the desired states, starting from the aerostatic situation
 1149 (marked by a cross). Besides that this would require a two hundred fold increase of Ψ , it
 1150 turns out that there is no continuation path (at $Re=\text{const}$) from the solid curve, where
 1151 $\Psi=1$, to the dashed curve, where $Re_g=-17.27$. This is shown in panel 20b, representing
 1152 a continuation of travelling-wave solutions at $Re=15.72$, where we have varied Re_g . The
 1153 solution curve exhibits a limit point at $Re_g \approx -10$ that precludes reaching the target value
 1154 $Re_g=-17.27$.

1155 We have also performed a transient computation on an open domain with inlet/outlet
 1156 conditions, where we have set $Re=15.72$ and forced waves of frequency $f=f_{\max}(Re_g =$

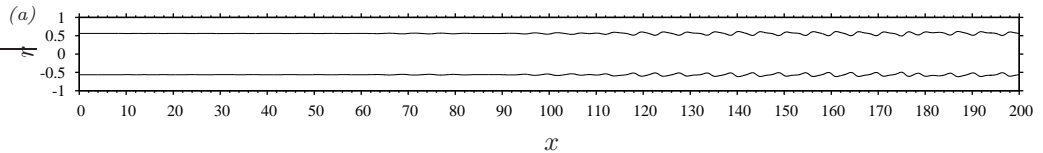


FIGURE 21. Version of the computation from panel 4a with axial viscous diffusion deactivated: $J_j=K_j=L_j=M_j=0$ in (2.5). The film surface is represented at the same time as in panel 4a.

1157 $-17.27)=0.73$, while gradually increasing Ψ from $\Psi=1$ according to a sigmoid function.
 1158 This computation produces occlusion long before Ψ has reached the target value $\Psi=237$,
 1159 which corresponds to the upper solution branch in panel 20a. We may thus conclude that
 1160 Re_{\max} , which is based on the limit point (LP) in panel 13a, remains a representative
 1161 occlusion bound also in the counter-current configuration.

1162 **Appendix D: Effect of axial viscous diffusion in panel 4a**

1163 Figure 21 represents a version of the computation from panel 4a where we have
 1164 deactivated axial viscous diffusion, by setting $J_j=K_j=L_j=M_j=0$ in (2.5b). In contrast
 1165 to panel 4a, no occlusion is observed over the entire length of the tube, which is in
 1166 qualitative contradiction with the experiments of Camassa *et al.* (2014).

1167 **Appendix E: Improved representation of liquid plugs**

1168 Inspired by the use of an additional attractive-repulsive force term to model contact
 1169 line problems within the framework of film models (Thiele *et al.* 2001), we add a repulsive
 1170 azimuthal capillary term to the RHS of our model equation (2.5b):

$$1171 \Pi_\theta = \text{We}^{-1} \exp \left[\lambda \left(1 - \frac{d(x,t)}{d_{\text{plug}}} \right) \right] \partial_x \kappa_\theta, \quad \kappa_\theta = -\frac{1}{d} \left[1 - \frac{1}{2} (\partial_x d)^2 \right]. \quad (4.1)$$

1172 As a result of its exponential variation with d (which can be scaled with λ), the effect of
 1173 this term is significant only in the vicinity of the predefined radius d_{plug} , which is set to
 1174 a small fraction of the tube radius R . At $d=d_{\text{plug}}$, Π_θ exactly compensates the capillary
 1175 pressure gradient due to (destabilizing) azimuthal curvature. Furthermore, by adequately
 1176 choosing d_{plug} and λ , the primary flow with a cylindrical film surface at $d=d_{\text{plug}}$ can be
 1177 rendered linearly stable at all wave numbers (we have checked this with spatial linear
 1178 stability analysis). This allows representing liquid plugs as stable travelling liquid annuli,
 or pseudo-plugs, that almost entirely fill the tube cross section.

1179 Figure 22 represents results of a transient periodic computation based on our WRIBL
 1180 model (2.5) with the additional force term Π_θ (4.1). Liquid properties and tube radius
 1181 correspond to case 4, which, due to the relevance of inertia, is the most challenging.
 1182 Further, $A=5.40$, $V_1/\pi/R^3=2.80$, $d_{\text{plug}}=0.01R$, and $\lambda=1$. Panel 22a represents the time
 1183 evolution of the film surface during formation of a pseudo-plug, and panel 22b represents
 1184 the fully-developed pseudo-plug. To better guide the eye, we have reproduced and shifted
 1185 the periodic surface profile in these panels.

1186 In contrast to the crude numerical core radius limitation employed in our open-domain
 1187 computations, our improved representation of liquid plugs ensures volume conservation,
 1188 and thus the pseudo-plug in figure 22 does not reopen. On the downside, this new repre-
 1189 sentation requires a finer spatial numerical resolution. Thus, open-domain computations,
 1190 such as the one in panel 17a, become more costly (about four times for case 4). This can

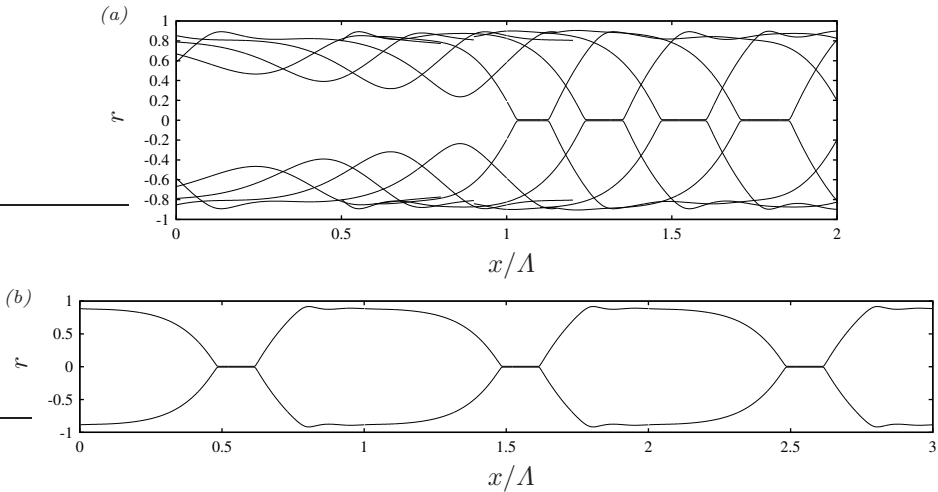


FIGURE 22. Improved representation of liquid plugs. Transient periodic computation based on the WRIBL model (2.5) upgraded with the localized repulsive term Π_θ (4.1), using $d_{\text{plug}}=0.01R$ and $\lambda=1$. Case 4: $\Lambda=5.40$; $V_1/\pi/R^3=2.80$. (a) Surface profiles at times $t^*/t_v^*=20, 30, 40, 50, 60, 70, 80, 90$ ($t_v^*=\nu_1^{1/3}g^{-2/3}=0.0037$ s), during the formation of a pseudo-plug. The four last profiles have been shifted by one wavelength to better guide the eye; (b) fully developed pseudo-plugs: $t^*/t_v^*=300$. The periodic surface profile has been reproduced three times here.

1191 be alleviated by implementing a locally refined grid in the plug regions, following the
 1192 example of Lister *et al.* (2006) for the representation of locally thin liquid films. We leave
 1193 this task, and the confrontation of our pseudo-plug model with full-fledged plug models
 1194 for pressure driven core-annular flows (Ubal *et al.* 2008) or inclined planar channel flows
 1195 (Suresh & Grotberg 2005), to future work. In the latter case, our additional force term
 1196 (4.1) would have to be adapted to a planar geometry.

1197 Acknowledgements

1198 This work was supported by the ANR wavyFILM project, grant ANR-15-CE06-0016-01
 1199 of the French Agence Nationale de la Recherche. Declaration of Interests. The authors
 1200 report no conflict of interest.

REFERENCES

- 1201 ALBERT, C., MARSCHALL, H. & BOTHE, D. 2013 Direct numerical simulation of interfacial mass
 1202 transfer into falling films. *International Journal of Heat and Mass Transfer* **69**, 343–357.
 1203 ALEKSEENKO, S. V., AKTERSHEV, S. P., CHERDANTSEV, A. V., KHARLAMOV, S. M. &
 1204 MARKOVICH, D. M. 2009 Primary instabilities of liquid film flow sheared by turbulent
 1205 gas stream. *International Journal of Multiphase Flow* **35**, 617–627.
 1206 AUL, R. W. & OLBRICHT, W. L. 1990 Stability of a thin annular film in pressure-driven,
 1207 low-reynolds-number flow through a capillary. *J. Fluid Mech.* **215**, 585–599.
 1208 BELTRAME, P. 2018 Partial and complete wetting in a micro-tube. *Europhysics Letters* **121**,
 1209 64002.
 1210 BENNEY, D. J. 1966 Long waves on liquid films. *Journal of Mathematics and Physics* **45**, 150–
 1211 155.
 1212 BIAN, S., TAI, C.-F., HALPERN, D., ZHENG, Y. & GROTBORG, J. B. 2010 Experimental study
 1213 of flow fields in an airway closure model. *Journal of Fluid Mechanics* **647**, 391–402.

- 1214 BRACKBILL, J. U., KOTHE, D. B. & ZEMACH, C. 1992 A continuum method for modelling
1215 surface tension. *J. Comput. Phys.* **100**, 335–354.
- 1216 BROOKE BENJAMIN, T. 1957 Wave formation in laminar flow down an inclined plane. *J. Fluid*
1217 *Mech.* **2**, 554–574.
- 1218 CAMASSA, R., FOREST, M. G., LEE, L., OGROSKY, H. R. & OLANDER, J. 2012 Ring waves
1219 as a mass transport mechanism in air-driven core-annular flows. *Phys. Rev. E* **86** (6),
1220 066305.
- 1221 CAMASSA, R., MARZUOLA, J. L., OGROSKY, H. R. & VAUGHN, N. 2016 Traveling waves for a
1222 model of gravity-driven film flows in cylindrical domains. *Physica D* **333**, 254–265.
- 1223 CAMASSA, R., OGROSKY, H. R. & OLANDER, J. 2014 Viscous film-flow coating the interior of
1224 a vertical tube. part 1. gravity-driven flow. *Journal of Fluid Mechanics* **745**, 682–715.
- 1225 CAMASSA, R., OGROSKY, H. R. & OLANDER, J. 2017 Viscous film-flow coating the interior of
1226 a vertical tube. part 2. air-driven flow. *Journal of Fluid Mechanics* **825**, 1056–1090.
- 1227 CHANG, H. C., DEMEKHIN, E. A. & KALADIN, E. 1996a Simulation of noise-driven wave
1228 dynamics on a falling film. *AIChE J.* **42** (6), 1553–1568.
- 1229 CHANG, H. C., DEMEKHIN, E. A., KALADIN, E. & YE, Y. 1996b Coarsening dynamics of
1230 falling-film solitary waves. *Phys. Rev. E* **54** (2), 1467–1477.
- 1231 CHANG, H. C., DEMEKHIN, E. A. & KOPELEVICH, D. I. 1993 Nonlinear evolution of waves on
1232 a vertically falling film. *Journal of Fluid Mechanics* **250**, 433–480.
- 1233 DAO, E. K. & BALAKOTAIAH, V. 2000 Experimental study of wave occlusion on falling films in
1234 a vertical pipe. *AIChE J.* **46** (7), 1300.
- 1235 DELAUNAY, C. 1841 Sur la surface de révolution dont la courbure moyenne est constante. *Journal*
1236 *de Mathématiques Pures et Appliquées* **6**, 309–320.
- 1237 DIETZE, G. F. 2016 On the Kapitza instability and the generation of capillary waves. *Journal*
1238 *of Fluid Mechanics* **789**, 368–401.
- 1239 DIETZE, G. F. 2019 Effect of wall corrugations on scalar transfer to a wavy falling liquid film.
1240 *Journal of Fluid Mechanics* **859**, 1098–1128.
- 1241 DIETZE, G. F. & RUYER-QUIL, C. 2013 Wavy liquid films in interaction with a confined laminar
1242 gas flow. *J. Fluid Mech.* **722**, 348–393.
- 1243 DIETZE, G. F. & RUYER-QUIL, C. 2015 Films in narrow tubes. *Journal of Fluid Mechanics*
1244 **762**, 68–109.
- 1245 DING, Z., LIU, Z., LIU, R. & YANG, C. 2019 Thermocapillary effect on the dynamics of
1246 liquid films coating the interior surface of a tube. *International Journal of Heat and Mass*
1247 *Transfer* **138**, 524–533.
- 1248 DOEDEL, E. J. 2008 AUTO07P: Continuation and bifurcation software for ordinary differential
1249 equations. *Montreal Concordia University* .
- 1250 DUPRAT, C., RUYER-QUIL, C., KALLIADASIS, S. & GIORGIUTTI-DAUPHINÉ, F. 2007 Absolute
1251 and convective instabilities of a viscous film flowing down a vertical fiber. *Physical Review*
1252 *Letters* **98**, 244502.
- 1253 EVERETT, D. H. & HAYNES, J. M. 1972 Model studies of capillary condensation. *J. Colloid*
1254 *Interface Sci.* **38** (1), 125–137.
- 1255 FRENKEL, A. L., BABCHIN, A. J., LEVICH, B. G., SHLANG, T. & SIVASHINSKY, G. I. 1987
1256 Annular flows can keep unstable films from breakup: nonlinear saturation of capillary
1257 instability. *J. Colloid Interface Sci.* **115** (1), 225–233.
- 1258 GAUGLITZ 1988 An extended evolution equation for liquid film breakup in cylindrical capillaries.
1259 *Chem. Eng. Sci.* **43** (7).
- 1260 GOREN, S. L. 1962 The instability of an annular thread of fluid. *J. Fluid Mech.* **12** (2), 309–319.
- 1261 GROTEBERG, J. 2011 Respiratory fluid mechanics. *Phys. Fluids* **23**, 021301.
- 1262 HICKOX, C. E. 1971 Instability due to viscosity and density stratification in axisymmetric pipe
1263 flow. *Phys. Fluids* **14** (2), 251–262.
- 1264 HIRT, C. W. & NICHOLS, B. D. 1981 Volume of fluid (VOF) method for the dynamics of free
1265 boundaries. *J. Comput. Phys.* **39**, 201–225.
- 1266 JENSEN, O. E. 2000 Draining collars and lenses in liquid-lined vertical tubes. *J. Colloid Interface*
1267 *Sci.* **221**, 38–49.
- 1268 JOSEPH, D. D., CHEN, K. P. & RENARDY, Y. Y. 1997 Core-annular flows. *Annu. Rev. Fluid*
1269 *Mech.* **29**, 65–90.

- 1270 KALLIADASIS, S. & CHANG, H. C. 1994 Drop formation during coating of vertical fibres. *Journal*
1271 *of Fluid Mechanics* **261**, 135–168.
- 1272 KALLIADASIS, S., RUYER-QUIL, C., SCHEID, B. & VELARDE, M. G. 2012 *Falling Liquid Films*,
1273 *Applied Mathematical Sciences*, vol. 176. Springer Verlag.
- 1274 KAMM, R. D. & SCHROTER, R. C. 1989 Is airway closure caused by a liquid film instability?
1275 *Respiration Physiology* **75**, 141–156.
- 1276 KAPITZA, P. L. 1948 Wave flow of thin layer of viscous fluid (in Russian). *Zhurn. Eksper. Teor.*
1277 *Fiz.* **18** (1), 3–28.
- 1278 KING, M. & MACKLEM, P. T. 1977 Rheological properties of microliter quantities of normal
1279 mucus. *Journal of Applied Physiology* **42** (6), 797–802.
- 1280 KOURIS, C. & TSAMOPOULOS, J. 2001 Dynamics of axisymmetric core-annular flow in a straight
1281 tube. I. the more viscous fluid in the core, bamboo waves. *Phys. Fluids* **13** (4), 841–858.
- 1282 LAVALLE, G., GRENIER, N., MERGUI, S. & DIETZE, G. F. to be published Solitary waves on
1283 superconfined falling liquid films. *Physical Review Fluids* .
- 1284 LEWIS, T. A., TZENG, Y.-S. AND MCKINSTRY, E. L., TOOKER, A. C., HONG, K., SUN, Y.,
1285 MANSOUR, J., HANDLER, Z. & ALBERT, M. S. 2005 Quantification of airway diameters
1286 and 3d airway tree rendering from dynamic hyperpolarized ³He magnetic resonance
1287 imaging. *Magnetic Resonance in Medicine* **53**, 474–478.
- 1288 LISTER, J. R., RALLISON, J. M., KING, A. A., CUMMINGS, L. J. & JENSEN, O. E. 2006
1289 Capillary drainage of an annular film: the dynamics of collars and lobes. *J. Fluid Mech.*
1290 **552**, 311–343.
- 1291 LIU, J. & GOLLUB, J. P. 1993 Onset of spatially chaotic waves on flowing films. *Physical Review*
1292 *Letters* **70** (15), 2289–2292.
- 1293 LIU, R. & DING, Z. 2017 Stability of viscous film flow coating the interior of a vertical tube
1294 with a porous wall. *Physical Review E* **95** (5), 053101.
- 1295 MATHEMATICA 2014 *Version 10.0.2.0*. Wolfram Research, Inc., Champaign, IL.
- 1296 NOSOKO, T., YOSHIMURA, P. N., NAGATA, T. & OYAKAWA, K. 1996 Characteristics of two-
1297 dimensional waves on a falling liquid film. *Chemical Engineering Science* **51** (5), 725–732.
- 1298 PLATEAU, J. P. 1849 Recherches expérimentales et théorique sur les figures d'équilibre d'une
1299 masse liquide sans pesanteur. *Mémoires de l'Académie Royale des Sciences, des Lettres et*
1300 *des Beaux-Arts de Belgique* **23**, 1–1.
- 1301 POPINET, S. 2009 An accurate adaptive solver for surface-tension-driven interfacial flows. *J.*
1302 *Comput. Phys.* **228**, 5838–5866.
- 1303 QUÉRÉ, D. 1990 Thin films flowing on vertical fibers. *Europhysics Letters* **13** (8), 721–726.
- 1304 QUÉRÉ, D. 1999 Fluid coating on a fibre. *Annu. Rev. Fluid Mech.* **31**, 347–384.
- 1305 RAYLEIGH, LORD 1892 On the instability of cylindrical fluid surfaces. *Philosophical Magazine*
1306 **34** (207), 177–180.
- 1307 RICHARD, G., RUYER-QUIL, C. & VILA, J. P. 2016 A three-equation model for thin films down
1308 an inclined plane. *Journal of Fluid Mechanics* **804**, 162–200.
- 1309 SEEBAUER, F., POECHLAUER, P., BRAUNE, S. & STEINHOFFER, S. 2012 Tube bundle falling film
1310 microreactor for performing gas liquid reactions. *US Patent* **8221708B2**.
- 1311 SHKADOV, V. YA. 1967 Wave flow regimes of a thin layer of viscous fluid subject to gravity.
1312 *Fluid Dyn.* **2** (1), 29–34.
- 1313 SURESH, V. & GROTEBERG, J. B. 2005 The effect of gravity on liquid plug
1314 propagation in a two-dimensional channel. *Physics of Fluids* **17** (3), 031507, arXiv:
1315 <https://doi.org/10.1063/1.1863853>.
- 1316 THIELE, U., VELARDE, M. G., NEUFFER, K & POMEAU, Y. 2001 Sliding drops in the diffuse
1317 interface model coupled to hydrodynamics. *Physical Review E* **64** (6), 061601.
- 1318 TRIFONOV, Y. Y. 1992 Steady-state traveling waves on the surface of a viscous liquid film falling
1319 down on vertical wires and tubes. *AIChE J.* **38** (6), 821–834.
- 1320 TRIFONOV, Y. Y. 2010 Counter-current gas-liquid wavy film flow between the vertical plates
1321 analyzed using the Navier-Stokes equations. *AIChE Journal* **56** (8), 1975–1987.
- 1322 TSELUIKO, D. & KALLIADASIS, S. 2011 Nonlinear waves in counter-current gas-liquid film flow.
1323 *J. Fluid Mech.* **673**, 19–59.
- 1324 UBAL, S., CAMPANA, D. M., GIAVEDONI, M. D. & SAITA, F. A. 2008 Stability of the steady-
1325 state displacement of a liquid plug driven by a constant pressure difference along a
1326 prewetted capillary tube. *Industrial & Engineering Chemistry Research* **47**, 6307–6315.

- 1327 VLACHOS, N. A., PARAS, S. V., MOUZA, A. A. & KARABELAS, A. J. 2001 Visual observations
1328 of flooding in narrow rectangular channels. *Int. J. Multiphase Flow* **27**, 1415–1430.
- 1329 WRAY, A. W. 2013 Electrostatically controlled large-amplitude, non-axisymmetric waves in thin
1330 film flows down a cylinder. *J. Fluid Mech.* **736**, R2.
- 1331 XU, F. & JENSEN, O. 2017 Trapping and displacement of liquid collars and plugs in rough-walled
1332 tubes. *Physical Review Fluids* **2**, 094004.
- 1333 YIH, C. S. 1963 Stability of liquid flow down an inclined plane. *The Physics of Fluids* **6** (3),
1334 321–334.
- 1335 YOSHIMURA, P. N., NOSOKO, P. & NAGATA, T. 1996 Enhancement of mass transfer
1336 into a falling laminar liquid film by two-dimensional surface waves-some experimental
1337 observations and modeling. *Chemical Engineering Science* **51** (8), 1231–1240.
- 1338 ZAPKE, A. & KRÖGER, D. G. 2000 Countercurrent gas-liquid flow in inclined and vertical
1339 ducts - I: Flow patterns, pressure drop characteristics and flooding. *International Journal*
1340 *of Multiphase Flow* **26**, 1439–1455.
- 1341 ZHOU, Z.-Q., PENG, J. & ZHANG, Y.-J. ZHUGE, W.-L. 2016 Viscoelastic liquid film flowing
1342 down a flexible tube. *Journal of Fluid Mechanics* **802**, 583–610.